

Radiofrequency Losses in an NMR Surface Coil

by

Mark D. Skubis

B.S., Physics
United States Naval Academy, 1996

Submitted to the Department of Nuclear Engineering
in partial Fulfillment of the Requirements for the Degree of
Master of Science in Nuclear Engineering

at the

Massachusetts Institute of Technology

June 1998

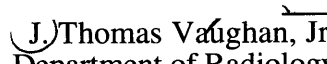
© 1998 Mark D. Skubis
All rights reserved

The author hereby grants to MIT permission to reproduce and to distribute publicly
paper and electronic copies of this thesis document in whole or in part.

Signature of Author _____

Department of Nuclear Engineering
8 May 1998

Certified by _____


Assistant Professor, Department of Radiology
Harvard Medical School
Thesis Supervisor

Certified by _____


Professor of Nuclear Engineering
Thesis Supervisor

Approved by _____


Lawrence Lidsky
Chairman, Department Committee on Graduate Students

AUG 18 1998 Science

Radiofrequency Losses in an NMR Surface Coil

by

Mark D. Skubis

Submitted to the Department of Nuclear Engineering
on 8 May 1998 in partial fulfillment of the
requirements for the Degree of Master of Science in
Nuclear Engineering

ABSTRACT

Radiofrequency energy loss has been investigated for a resonant NMR surface coil between 20 MHz and 400 MHz. High-field NMR (> 64 MHz) is used increasingly for human imaging and spectroscopy to achieve improved SNR and spectral resolution. RF losses in coils designed using conventional lumped-element principles, however, often limit the practicality of high-field imaging. New design principles are required for the construction of *efficient* high-field RF coils.

The RF energy losses investigated include RF coil losses and losses to a phantom load. These were studied using single-loop, resonant surface coils. Coil Q values, both unloaded and loaded, were measured and used to determine the coil radiation resistance, load resistance, B_1 field magnitude, and SNR. Radiation resistance is shown to increase like $R_r \sim f_o^4$.

It is widely believed that load losses dominate all other losses in biomedical NMR. This study indicates that limiting radiation losses may improve loaded coil SNR at high frequencies. To this end, one may decrease the coil electrical length and/or apply transmission line principles in the construction of RF coils. Decreasing the coil electrical wavelength may be accomplished by decreasing the coil dimensions. Transmission line principles, which have been demonstrated for volume coils, improve performance by minimizing the coil radiation resistance.

Thesis Supervisor: J. Thomas Vaughan, Jr.

Title: Assistant Professor, Department of Radiology
Harvard Medical School

Thesis Supervisor: David Cory

Title: Professor of Nuclear Engineering

TABLE OF CONTENTS

Abstract	2
Table of Contents	3
1. Introduction	4
2. Background	6
3. Theory	8
4. Materials and Methods	28
5. Results	33
6. Discussion	38
7. Applications	44
8. Conclusions	48
Acknowledgments	50
Appendix A: Abbreviations and symbols	51
Appendix B: Q data	56
References	58

1. INTRODUCTION

There is considerable movement to high static magnetic fields (B_0 fields) in nuclear magnetic resonance (NMR) experiments (1-22). This trend is motivated by the greater signal-to-noise ratio (SNR) and enhanced spectral resolution obtained at higher fields¹. In an electrically lossless sample under ideal conditions, Hoult predicts SNR increases with frequency like $f_0^{(7/4)}$ ² (23), and for an electrically lossy sample, such as physiologic tissue, he estimates SNR increases approximately linearly with frequency (23). SNR gains are desirable as they may be used to enhance the spatial resolution, temporal resolution, or contrast-to-noise ratio (CNR) of NMR images. Figure 1 shows the improvement in SNR and spectral resolution obtained with increasing field strength.

This investigation will show that the SNR benefit sought by moving to higher frequencies may be diminished by radiofrequency-dependent energy losses. For loaded coils, the primary sources of radiofrequency (RF) energy loss are the ohmic (R_Ω [Ω]), radiation (R_r [Ω]), and tissue load (R_L [Ω]) resistances. These affect SNR with increasing angular frequency, ω ($\omega = 2\pi f$), like (23)

$$\text{SNR} \sim \frac{\omega^2 \kappa(\mathbf{r})}{\sqrt{R_\Omega + R_r + R_L}} = \frac{\omega^2 \kappa(\mathbf{r})}{\sqrt{R}} \quad [1]$$

where $\kappa(\mathbf{r})$ is the magnitude of the signal-generating RF field (B_1 [T]) per unit current. As frequency increases R simultaneously grows, diminishing the SNR gains realized with increasing ω .

¹ For this study *high field* is considered a magnetic field greater than 1.5 T.

² B_0 [T] and f_0 [MHz] are directly related by the nuclear gyromagnetic ratio, γ [MHz/T], such that $f_0 = \gamma B_0$. This is known as the Larmor relation.

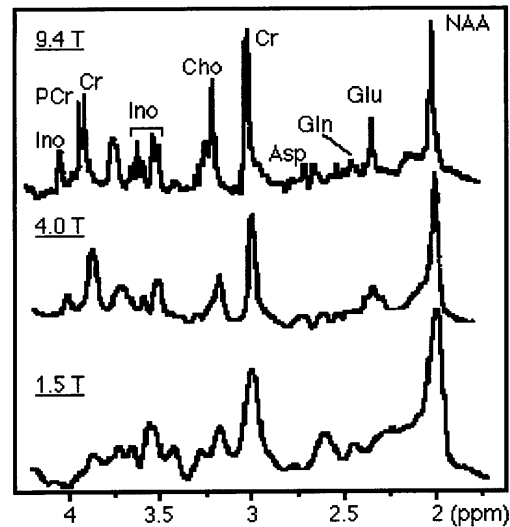


Figure 1. The increase in SNR and spectral resolution with increasing B_0 . The spectra were collected in similar NMR surface coil spectroscopy experiments performed on canine brains *in-vivo* at 1.5, 4.0, and 9.4 T at the University of Minnesota [24].

The aforementioned RF energy losses become a significant obstacle to high-field experiments when the RF coil(s), which generate the B_1 field, are designed using lumped-element (RLC) equations. The electrical length of the lumped-element coil increases as frequency increases. This causes the coil to behave less like an energy-conserving *coil* and more like an energy-radiating *antenna*. As with any well-designed antenna, more power is radiated from the RF coil to the surroundings. While this increase in radiated energy is desirable for antennae, an efficient coil must radiate as little energy as possible in order to stimulate and receive a detectable NMR signal.

Currently, the mechanisms and parameters affecting RF losses are not well-characterized. The goal of this study is, therefore, to better understand basic RF coil performance versus frequency. To this end, we use single-loop, resonant surface coils to investigate the frequency dependence of the coil Q, B_1 field strength, and SNR. This yields quantitative information about RF losses that may subsequently be used to indicate design principles appropriate for constructing *efficient* high-field RF coils, including surface coils, phased arrays, and volume coils.

2. BACKGROUND

In 1946 both Purcell (25) and Bloch (26) reported the detection of an NMR signal. NMR was immediately applied to chemical spectroscopy, but it took decades before the first NMR image was formed (27). In 1973, Lauterbur (27) and Mansfield (28) both realized how to spatially localize the NMR signal, making NMR imaging a reality. Soon after Lauterbur's first image, whole-body human images were able to be constructed (29,30). As the first NMR imaging experiments were being performed on humans, theoreticians explored ways to improve the imaging process. They posited that increased SNR and higher spectral resolution would be obtained by moving to higher B_0 fields (23).

Scientists were eager to explore the possible gains in SNR, so NMR magnet technology rapidly progressed. In the 1980's, biomedical NMR research was dominated by mid- and high-field magnets with B_0 values as high as 4.1 T (22). Clinical NMR scanners evolved, too--whole-body magnets up to 2.0 T were available (31). Finally, the early 1990's saw the clinical NMR scanner settle at $B_0 = 1.5$ T. This occurred due to 1) high-field technological limitations, 2) high-field costs, and 3) RF safety concerns. This continues to be the highest clinical field strength approved for use in the United States, as permitted by the Food and Drug Administration³.

Notwithstanding the current standards, interest in higher B_0 fields has existed for many years. In 1987 General Electric, Siemens, and Philips each built 4.0 T whole-body NMR systems to investigate potential high-field clinical applications (32). Human exposure to the 4.0 T static magnetic field was found to be safe (31), and early high-field experiments soon followed (22). Today, many studies have been safely performed at high fields (1-22,33) and the improvement in spectral, spatial, and temporal resolution is well-documented (21). High-field imaging is now used extensively in human anatomic, metabolic, and functional applications for both diagnostic and research purposes (1-20).

³ General Electric is currently seeking FDA approval for its 3.0 T clinical imaging system.

Widely-reported successes at high fields have prompted many medical research centers to acquire high-field NMR scanners. There are currently thirty-six 3.0 to 4.0 T whole-body magnets worldwide used for biomedical research while whole-body magnets as high as 8.0 T have recently been delivered to research institutions. However, as magnet strength and the dependent Larmor frequency increase, the radiation resistance of the RF coil theoretically increases like f_0^4 (34-37). That is to say, the power radiated by the coil rapidly increases, leading to a diminished signal. Apparently, limiting radiation resistance should be a high priority in ensuring *efficient* high-field biomedical applications. This necessity was recognized in early high-field studies and is now firmly established (38-40).

The deteriorating performance of conventional RF coils at high frequencies may be explained by antenna theory. The RF wavelength and the diameter of an RF surface coil loop are defined as λ [m] and D [m], respectively. As a rule of thumb, the diameter of an *efficient* RF surface coil loop (*i.e.* one that retains 99% of its energy) may not exceed 0.1λ (35). When the coil exceeds that dimension, it is not *electrically small*. Its behavior increasingly resembles that of an antenna, radiating energy rather than conserving it. Table 1 illustrates how the coil diameter, relative to λ , increases as B_0 increases.

Because of their radiating behavior, coils designed using traditional lumped-element design equations exhibit deteriorating performance, both theoretically and experimentally, as frequency increases (36,41-43). In many cases, the RF coil cannot even be tuned to the desired resonant frequency. This study will examine and quantify the effects of RF losses. These efforts will permit the outline of general guidelines for constructing efficient high-field RF coils.

Table 1. Increase in the RF coil diameter in terms of the resonant RF wavelength. The calculations assume a circular surface coil with $D = 20$ cm. When $D > 0.1\lambda$, the coil radiative losses are no longer negligible (35).

B_0 field strength (T)	^1H resonance frequency (MHz)	λ (cm)	Coil length
0.5	21	1428	0.01λ
1.5	64	468	0.04λ
3.0	128	234	0.08λ
4.7	200	150	0.13λ
7.0	300	100	0.20λ
9.4	400	75	0.26λ

3. THEORY

3.1 NMR THEORY

The *nuclear spin*, \mathbf{I} [J·s], is given by (44)

$$\mathbf{I} = \sum_{i=1}^A (\mathbf{l}_i + \mathbf{s}_i), \quad [2]$$

where \mathbf{l}_i [J·s] is the classical orbital angular momentum of each nucleon, \mathbf{s}_i [J·s] is the spin angular momentum of each nucleon, and A is the atomic number. The nuclear spin obeys the standard quantum mechanical relationships for angular momentum, *vis.* (44)

$$|\mathbf{I}| = \sqrt{I(I+1)} \left(\frac{h}{2\pi} \right) \quad [3]$$

and

$$I_z = m_I \left(\frac{h}{2\pi} \right), \quad (m_I = I, I-1, \dots, 1-I, -I) \quad [4]$$

where I is the nuclear spin quantum number, h [J·s] is Planck's constant, and I_z [J·s] is the component of the nuclear spin along the z -axis. For ^1H in the ground energy state, $I = 1/2$ as determined by the single proton in the nucleus. Therefore

$$I_z = \pm \frac{1}{2} \left(\frac{h}{2\pi} \right). \quad [5]$$

The current distribution in a $I = 1/2$ nucleus is spherically symmetric (44). Thus, the first nonvanishing term in the multipole expansion for $I = 1/2$ nuclei is the magnetic dipole moment (44). Interactions of these type nuclei with electromagnetic fields are primarily magnetic. Accordingly, NMR experiments focus on observation of $I = 1/2$ nuclei as there are no unwanted higher-order multipole interactions.

The nuclear magnetic moment ($\mu_{I,z}$ [A·m²]), which is defined as parallel to the z -axis, is related to the nuclear spin such that (45)

$$\mu_{I,z} = \gamma I_z \left(\frac{h}{2\pi} \right) = \pm \frac{1}{2} \gamma \left(\frac{h}{2\pi} \right). \quad [6]$$

For $I = 1/2$ nuclei, it is clear from [6] that the gyromagnetic ratio of the nuclear species determines the strength of $\mu_{1,z}$, which in turn determines the sensitivity to detection of the nuclei in the sample. Protons have the largest gyromagnetic ratio save the unstable tritium (^3H) nucleus (Table 2 displays the gyromagnetic ratios of commonly observed nuclei in NMR). Furthermore, because hydrogen is the most abundant nucleus in biological systems, signal-producing protons are numerous. For these reasons, ^1H is the most frequently observed nucleus in NMR (45).

Table 2. The gyromagnetic ratios of nuclei commonly observed in NMR (45).

Nucleus	Gyromagnetic ratio [γ] (MHz/T)	Relative sensitivity*	Resonance frequency at 1.5T (MHz)
^1H	42.58	1	64
^{13}C	10.71	0.016	16
^{19}F	40.05	0.830	60
^{23}Na	11.26	0.093	17
^{31}P	17.23	0.066	26
^{39}K	1.99	$5.08(10^{-4})$	3

* Calculated at a constant magnetic field for equal numbers of nuclei

The potential energy E [J] of a magnetic moment μ [$\text{A}\cdot\text{m}^2$] in an external magnetic field \mathbf{B} [T] is (45)

$$E = -\mu \cdot \mathbf{B} \quad [7]$$

If we stipulate that the applied B_0 field is parallel to the z-axis, then [7] may be simplified to

$$E = -\mu_{1,z} B_0 \quad [8]$$

For $I = 1/2$ nuclei this results in a splitting of the ground state energy level, known as the Zeeman effect. Combining equations [6] and [8] shows that the two allowed ground state energies of a $I = 1/2$ nucleus are

$$E = \pm \frac{1}{2} \gamma B_0 \left(\frac{\hbar}{2\pi} \right) \quad [9]$$

and the energy difference between these two states, ΔE [J], is

$$\Delta E = E_+ - E_- = \gamma B_0 \left(\frac{\hbar}{2\pi} \right) \quad [10]$$

Substituting the Larmor relationship into [10] reveals

$$\Delta E = \hbar \omega \left(\frac{\hbar}{2\pi} \right) \quad [11]$$

Thus the difference between the two ground state energy levels of a $I = 1/2$ nucleus is directly proportional to the externally applied magnetic field (*i.e.* the nuclear resonant frequency).

3.2 RF COILS

The energy difference given in [11], which falls in the RF band of the electromagnetic spectrum, is exploited to produce the signal in the NMR experiment. The alternating electric current at an arbitrary point on the RF coil, $\mathbf{I}(\mathbf{r})$ [A], generates a time-dependent magnetic field at a field point according to (46)

$$\mathbf{B} = \nabla \times \mathbf{A} \quad [12]$$

where

$$\mathbf{A} = \frac{\mu_0}{4\pi} \int_{\text{coil}} \mathbf{I}(\mathbf{r}) \frac{e^{-jk r}}{r} d\mathbf{l} \quad [13]$$

\mathbf{A} [A/m] is the magnetic vector potential at the field point, μ_0 [N/A²] is the permeability of free space, $k^2 = \omega^2 \mu \epsilon$ (μ [N/A²] and ϵ [C²/N·m²] are the permeability and permittivity, respectively, of the surrounding medium), r [m] is the distance from the point on the coil to the field point, and $d\mathbf{l}$ [m] is an infinitesimal length element along the coil. Equation [13] is a line integral that must be performed around the entire coil to be complete.

The magnetic field given in [12] is the \mathbf{B}_1 field. This field, generated to oscillate at f_0 , is applied orthogonally to B_0 and so is simplified to its magnitude, B_1 . The B_1 field couples to the magnetic moment of the sample, which is a magnetic dipole oscillating at f_0 . The result of this configuration is the transfer of RF energy from the B_1 field to the sample spins. This energy transfer from the RF *transmitter* coil excites spins from the lower to the upper spin state.

The spins excited by the B_1 field are then allowed to return to their equilibrium state. The ensemble of all nuclear magnetic moments in a sample may be represented as a net magnetic moment, \mathbf{M} [A·m²], where

$$\mathbf{M} = \sum_{n=1}^{n_{\max}} \mu_{1,n} \quad [14]$$

n being the number of nuclei of interest in the sample. \mathbf{M} is subjected to a torque from the static magnetic field, given classically by (45)

$$\frac{d\mathbf{M}}{dt} = -\gamma(\mathbf{B}_o \times \mathbf{M}) \quad [15]$$

The resulting motion is a precession of \mathbf{M} at the Larmor frequency, f_o . This precession induces an emf in the RF *receiver* coil according to

$$\text{emf} = \int_{\text{coil}} \mathbf{E} \cdot d\mathbf{l} \quad [16]$$

where the electric field \mathbf{E} [V/m] is given by

$$\mathbf{E} = -\frac{\partial \mathbf{A}}{\partial t} \quad [17]$$

This line integral is evaluated around the coil for each infinitesimal length element $d\mathbf{l}$. The current resulting from the emf induced in the receiver coil is the signal that is detected in the NMR experiment.

The RF transmitter coil excites the nuclear spins to a higher energy state and the receiver coil carries the spin-induced current. Thus, the RF coils both *stimulate* and *detect* the NMR signal, making them an essential component in the NMR experiment. Any energy loss mechanisms affecting RF coil performance must be well-understood in order to realize efficient coil design.

3.3 RESONANT RF COIL LOOPS

Impedance is a barrier to current in an electrical circuit. The RF coil impedance is the input impedance, Z_{in} [Ω], or impedance measured across the coil terminals. For an unloaded coil, Z_{in} consists of a real and imaginary component (35),

$$Z_{in} = R_{in} + jX_{in}. \quad [18]$$

R_{in} [Ω] is the input resistance and is related to the average power dissipated in the coil, P_{in} [W], by (35)

$$P_{in} = \frac{1}{2} R_{in} |I_{in}|^2 \quad [19]$$

where I_{in} [A] is the peak current across the coil terminals. In free space, power dissipation may occur due to either coil ohmic losses (P_{Ω} [W]) or radiation losses (P_r [W]),

$$P_{in} = P_{\Omega} + P_r. \quad [20]$$

The input reactance of the coil, X_{in} [Ω], represents power stored in the electromagnetic field about the coil. Reactance in general consists of both a capacitive (X_C [Ω]) and an inductive (X_L [Ω]) component,

$$X = X_C + X_L. \quad [21]$$

Capacitive reactance is given by

$$X_c = \frac{1}{\omega C}, \quad [22]$$

where C [F] is the coil capacitance. The inductive reactive component is

$$X_L = \omega L, \quad [23]$$

where L [H] is the coil inductance.

Maximum coil efficiency, which yields the highest possible SNR, occurs when Z_{in} is minimized. If impedance is represented as a vector [R, X] in the complex plane, minimization of the vector magnitude occurs when $X = 0^4$. Coils with zero reactance are referred to as *resonant* and are constructed by balancing the capacitive and inductive reactance according to

$$X_L = X_c \quad [24]$$

$$\frac{1}{\omega C} = \omega L \quad [25]$$

$$\omega = \frac{1}{\sqrt{LC}}. \quad [26]$$

3.4 RF LOSS MECHANISMS

There are two primary sources of RF loss in the NMR experiment--coil losses and losses to the tissue load. RF coil losses, due to the input resistance of the coil, may be divided into losses

⁴ There is almost always some resistance, R, in the coil. This component of impedance cannot be eliminated.

due to the ohmic resistance (R_{Ω}) and radiation resistance (R_r) of the coil (33). Tissue losses include losses due to both eddy currents induced in the tissue conductor and displacement currents induced in the tissue dielectric (33).

3.4.1 RF COIL OHMIC LOSSES

The average power dissipated in a coil, P_{in} , was shown in [19] as (35)

$$P_{in} = \frac{1}{2} R_{in} |I_{in}|^2. \quad [27]$$

Equation [27] may be decomposed into the ohmic and radiative power loss, seen in [20], which may also be written as (35)

$$P_{in} = \frac{1}{2} R_{\Omega} |I_{in}|^2 + \frac{1}{2} R_r |I_{in}|^2. \quad [28]$$

The coil radiation resistance referenced to the input terminals, R_{ri} [Ω], is then defined as (35)

$$R_{ri} = \frac{2P_r}{|I_{in}|^2}. \quad [29]$$

The ohmic resistance of the coil is, therefore (35),

$$R_{\Omega} = \frac{2P_{\Omega}}{|I_{in}|^2} = \frac{2(P_{in} - P_r)}{|I_{in}|^2}. \quad [30]$$

The resistance of a wire carrying RF current is given by (35)

$$R_{\Omega} = \frac{\ell}{2\pi a} R_s, \quad [31]$$

where ℓ [m] is the wire length, a [m] is the wire radius, and R_s [Ω] is the surface resistance of the wire. The surface resistance reflects the fact that current flows primarily on the surface of the coil conductor in this instance and (35)

$$R_s = \sqrt{\frac{\omega\mu}{2\sigma}}, \quad [32]$$

where σ [$\Omega^{-1}\cdot\text{m}^{-1}$] is the coil conductivity. Combining equations [31] and [32] reveals that coil ohmic resistance increases proportionally with the square root of frequency,

$$R_{\Omega} = \frac{\ell}{2\pi a} \sqrt{\frac{\omega\mu}{2\sigma}} \quad [33]$$

$$R_{\Omega} \sim \omega^{1/2}. \quad [34]$$

The finite resistance of the capacitance (R_{cap} [Ω]) in the coil may be added to the ohmic resistance to determine the total resistive losses in the circuit. American Technical Ceramics (ATC), the manufacturer of the capacitors used in this study, has measured the resistance of their capacitors at various frequencies. Data were used to generate an algorithm written in Visual Basic code from which R_{cap} at a given frequency may be determined (47). R_{cap} values were calculated for the capacitances and frequencies of interest in this study and are displayed in Table 3⁵.

⁵ C is calculated from [26] using the coil inductance, described in §4.

Table 3. R_{cap} calculated by ATC software (47). All resistances were calculated for the 100E series microstrip capacitors.

^1H resonance frequency (MHz)	Capacitance (pF)	R_{cap} (Ω)
21	200	0.020
64	22	0.072
128	5.5	0.165
200	2.2	0.284
300	1.0	0.458
400	0.5	> 0.5

3.4.2 RF COIL RADIATIVE LOSSES

The radiation resistance of a coil referenced to the maximum coil current (R_r , [Ω]) is (35)

$$R_r = \frac{2P_r}{|I_{\text{in}}|^2} \quad [35]$$

For *electrically small* surface coils, the maximum coil current is across the coil terminals so $R_r = R_{\text{ii}}$ (35). The maximum dimension for the *electrically small* condition to apply is listed for several frequencies in Table 4.

The region satisfying the condition (46)

$$r < 0.62 \left(\frac{D^3}{\lambda} \right)^{1/2}, \quad [36]$$

where D [m] is the coil diameter and r [m] is the radius of a sphere originating at the coil center, is referred to as the near field. The energy stored in the near field is used to excite the sample spins

and generate signal. Radiation resistance allows reactive energy in the near field to be lost to the surroundings, including the patient, the magnet bore conductors, and free space. When energy is radiated from the near field, the coil becomes less efficient. This results in a diminished SNR.

Table 4. The maximum physical coil dimension permitted for the electrically small coil condition to apply.

Frequency (MHz)	λ (cm)	Maximum coil dimension (cm)
21	1428	142.8
64	468	46.8
128	234	23.4
200	150	15.0
300	100	10.0
400	75.0	7.50

Radiation resistance may be determined from [35] if one knows the power radiated by the coil, P_r [W]. Electromagnetic waves transport energy as they propagate. The instantaneous Poynting vector, \mathcal{S} [W/m²], describes the power density associated with an electromagnetic wave and is given by (46)

$$\mathcal{S} = \mathcal{E} \times \mathcal{H} \quad [37]$$

where \mathcal{E} [V/m] is the instantaneous electric field intensity and \mathcal{H} [A/m] is the instantaneous magnetic field intensity. The total instantaneous power, \mathcal{P} [W], passing through a closed surface is given by integration of the power density over the entire surface (46), *i.e.*

$$\mathfrak{P} = \int_{\text{surf}} \mathfrak{S} \cdot d\mathbf{s} = \int_{\text{surf}} (\mathfrak{S} \cdot \hat{\mathbf{n}}) da \quad [38]$$

where $\hat{\mathbf{n}}$ is the unit normal to the surface and da [m^2] is an infinitesimal area element on the surface. In this case the average cycle power divided by the cycle is useful, for the instantaneous fields vary with time. Time-dependent harmonic fields may be expressed in terms of the complex fields \mathbf{E} [V/m] and \mathbf{H} [A/m] (46):

$$\mathfrak{E}(x,y,z,t) = \text{Re} [\mathbf{E}(x,y,z) e^{j\omega t}] \quad [39]$$

$$\mathfrak{H}(x,y,z,t) = \text{Re} [\mathbf{H}(x,y,z) e^{j\omega t}]. \quad [40]$$

Using the identity (46)

$$\text{Re} [\mathbf{E}e^{j\omega t}] = \frac{1}{2} [\mathbf{E}e^{j\omega t} + \mathbf{E}^*e^{-j\omega t}] \quad [41]$$

one may write [37] as

$$\mathfrak{S} = \frac{1}{2} \text{Re} [\mathbf{E} \times \mathbf{H}^*] + \frac{1}{2} \text{Re} [\mathbf{E} \times \mathbf{H}e^{j2\omega t}] \quad [42]$$

The time-averaged Poynting vector, \mathbf{S}_{av} [W/m^2], may now be written as (46)

$$\mathbf{S}_{\text{av}}(x,y,z) = [\mathfrak{S}(x,y,z,t)]_{\text{av}} = \frac{1}{2} \text{Re} [\mathbf{E} \times \mathbf{H}^*]. \quad [43]$$

Based on this definition, the *time-averaged* radiated power, P_r , is (46)

$$P_r = P_{av} = \int_{\text{surf}} \mathbf{S}_{av} \cdot d\mathbf{s} = \frac{1}{2} \int_{\text{surf}} \text{Re} [\mathbf{E} \times \mathbf{H}^*] \cdot d\mathbf{s} \quad [44]$$

The real component of the radiated power is (35)

$$P_r = 10 I_{in}^2 (k^2 S)^2 \quad [45]$$

where S [m^2] is the coil area. Radiation resistance along a conductive copper surface in air may then be calculated by substituting [45] into [35] so (35)

$$R_r = \frac{2P_r}{I_{in}^2} = 20 (k^2 S)^2 \quad [46]$$

$$R_r \approx 31,200 \left(\frac{S}{\lambda^2} \right)^2 = 31,200 \frac{S^2 f^4}{c^4} \quad [47]$$

$$R_r \sim S^2 f^4, \quad [48]$$

revealing that radiation resistance increases with the size of the coil like S^2 and with frequency like f^4 . Equation [47] holds for any circular surface coil whose perimeter is less than 0.3λ (35).

Figure 2 shows that radiation resistance is the major contribution to the total resistance of the unloaded coil at higher frequencies. This implies that unloaded RF coil losses may be primarily attributed to the coil radiation resistance.

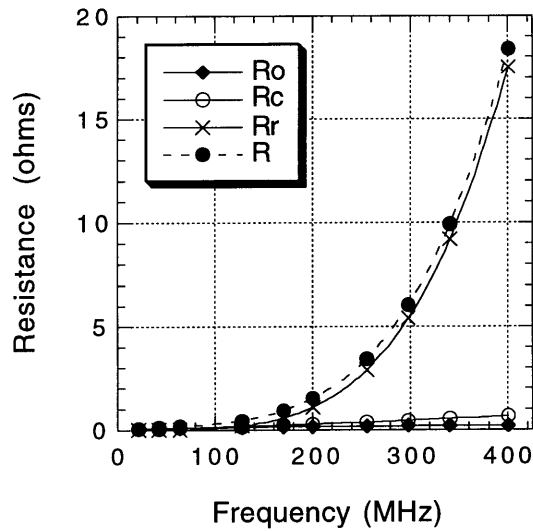


Figure 2. Ohmic resistance (R_o), capacitive resistance (R_c), radiation resistance (R_r), and total resistance (R) versus frequency for the surface coil described in Table 5. At higher frequencies the radiation resistance dominates the total coil resistance.

3.4.3 RF TISSUE LOSSES

The other major RF loss mechanisms are losses to the tissue load. Human tissue is a conductive and dielectric medium—electromagnetic fields in the vicinity of tissue will induce conductive currents and displacement currents. These patient-associated losses cannot be eliminated. In a lossy, anisotropic, inhomogeneous system of coil and tissue load, the losses are best described by time-dependent electromagnetic field equations. The B_1 field in this system is given by the Maxwell-Ampère Law (48),

$$\nabla \times \frac{\mathbf{B}_1}{\mu} = \mathbf{J}_c + \frac{\partial \mathbf{D}}{\partial t} \quad [49]$$

where \mathbf{J}_c [A/m^2] is the conduction current density and \mathbf{D} [C/m^2] is the electric flux density. Ohm's Law allows the conduction current density to be written as

$$\mathbf{J}_c = \sigma_L \mathbf{E}, \quad [50]$$

and Euler's Law allows us to express \mathbf{D} as (33)

$$\frac{\partial \mathbf{D}}{\partial t} = \frac{\partial \epsilon_L \mathbf{E}}{\partial t} = j\omega \epsilon_L \mathbf{E} \quad [51]$$

Using [50] and [51], [49] may be given as (33)

$$\nabla \times \frac{\mathbf{B}_1}{\mu} = (\sigma_L + j\omega \epsilon_L) \mathbf{E} \quad [52]$$

\mathbf{E} is a complex value that may be expressed in terms of the magnetic vector potential \mathbf{A} and the scalar potential ϕ [V] so (33)

$$\nabla \times \frac{\mathbf{B}_1}{\mu} = (\sigma_L + j\omega \epsilon_L) \cdot (-j\omega \mathbf{A} - \nabla \phi) \quad [53]$$

Equation [53] shows two sources of load loss in NMR. The B_1 -induced conduction (or eddy) current density goes according to (33)

$$\mathbf{J}_c = -j\omega \sigma_L \mathbf{A} \quad [54]$$

$$\mathbf{J}_c \sim \omega. \quad [55]$$

The displacement current density \mathbf{J}_d [A/m²] may be expressed as (33)

$$\mathbf{J}_d = -j\omega\epsilon_L\mathbf{E} = \omega^2\epsilon_L\mathbf{A} \quad [56]$$

$$\mathbf{J}_d \sim \omega^2. \quad [57]$$

These losses are load-specific as determined by the tissue conductivity and dielectric, σ_L [$\Omega^{-1}\cdot\text{m}^{-1}$] and ϵ_L [$\text{C}^2/\text{N}\cdot\text{m}^2$] (33).

3.5 RF COIL PERFORMANCE

The Q value, or quality factor, is a measure of coil *efficiency*. Q is a dimensionless figure of merit that is defined as the ratio of the energy stored to the energy dissipated in the coil circuit. This is given by (35)

$$Q = \frac{X_{in}}{R_{in}} \quad [58]$$

or, for an inductive coil loop,

$$Q = \frac{X_{in}}{R_{in}} = \frac{\omega L}{R}. \quad [59]$$

From the theoretical unloaded total resistance of the coil ($R = R_{\Omega} + R_{cap} + R_r$) and the coil inductor (see §4), one may calculate and plot the Q values versus frequency. This was done using a Microsoft Excel spreadsheet--the results are displayed in Figure 3.

An accurate indication of coil *performance* is the B_1 field, generated by the coil current, over a region of interest. From the discussion of §3.2, this field of the couples to the nuclear

magnetic moments, resulting in the NMR signal. The B_1 field will primarily determine both how well the excitation energy is delivered to the sample and how efficiently the NMR signal is then received. For a given power input, the coil current obeys the following relation:

$$P_{in} = I_{in}^2 R_{in} \quad [60]$$

so

$$I_{in} = \sqrt{\frac{P_{in}}{R_{in}}} \sim \frac{1}{\sqrt{R}} \quad [61]$$

Therefore, a relative measure of the B_1 field may be calculated from the Biot-Savart Law (49)

$$\mathbf{B} = \frac{\mu_0}{4\pi} \int_{coil} \frac{I d\mathbf{l} \times \hat{\mathbf{r}}}{r^2} \quad [62]$$

For a circular loop of radius b [m] at a distance r [m] along the axis normal to the plane of the coil and through the coil center, the magnetic field strength is (49)

$$B_1 = \frac{\mu_0}{4\pi} \frac{2\pi b^2 I_{in}}{(r^2 + b^2)^{3/2}} \quad [63]$$

$$B_1 \sim \frac{\mu_0}{4\pi} \frac{1}{\sqrt{R}} \frac{2\pi b^2}{(r^2 + b^2)^{3/2}} \quad [64]$$

$$B_1 \sim \frac{\kappa(\mathbf{r})}{\sqrt{R}} \quad [65]$$

where $\kappa(\mathbf{r})$ is a geometric factor. The calculated B_1 values are shown with increasing frequency in Figure 4.

SNR is the figure of merit for NMR coil applications, as it is directly related to image quality. SNR follows the general relation (23)

$$\text{SNR} \sim \frac{\omega^2 \kappa(\mathbf{r})}{\sqrt{R}}, \quad [66]$$

and its behavior with frequency for an unloaded coil is shown in Figure 5.

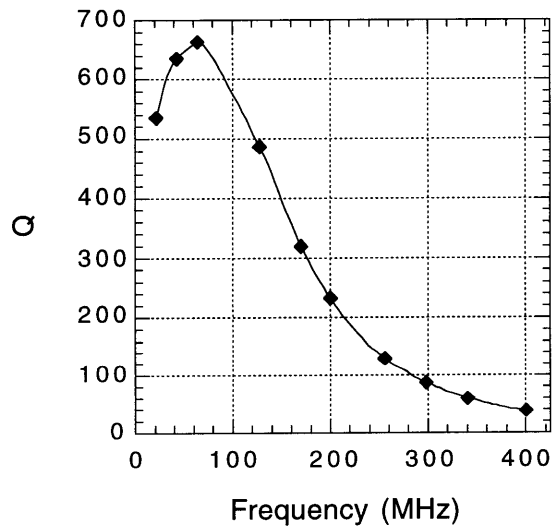


Figure 3. Unloaded Q versus frequency for the surface coil described in Table 5. Included are contributions from R_{Ω} , R_{cap} , and R_r .

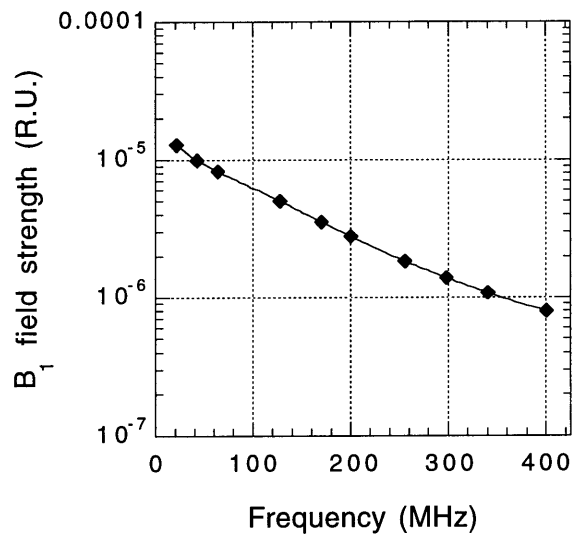


Figure 4. Unloaded B_1 field magnitude at one coil radius versus frequency for the surface coil described in Table 5. The units of B_1 are relative to a given power input.

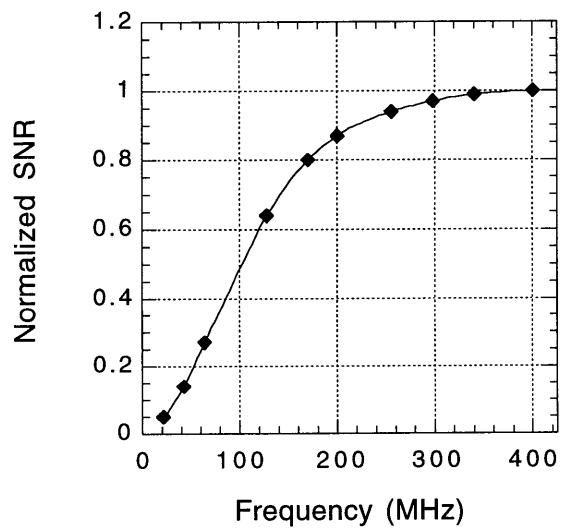


Figure 5. Unloaded, normalized SNR versus frequency for the surface coil described in Table 5.

4. MATERIALS AND METHODS

The benefits of RF surface coils are widely recognized (50-52) for localized, high-sensitivity signal acquisition, and surface coils are in abundant use in the biomedical NMR community (53-81). This general applicability, as well as its design simplicity, is why the single-loop surface coil was chosen for this study. What is learned about RF coil losses from this investigation applies to all NMR coils. Table 5 summarizes the surface coil characteristics. Coils were fabricated in three configurations: with coil capacitance (necessary to make resonant coils) distributed in one, two, and four locations. This was done with the intention of making the current distribution around the loop more uniform. Figure 6 shows schematic diagrams of the three coil configurations utilized.

Table 5. The design specifications of the surface coils used in this study.

coil material	copper
coil shape	circle
wire diameter	$d = 0.317 \text{ cm}$
wire length	$\ell = 40.89 \text{ cm}$
coil radius	$b = 6.50 \text{ cm}$

Small loop surface coils are inherently inductive (35). The inductance of a circular loop satisfying the condition $d \ll b$ is (35)

$$L = b\mu \left[\ln \left(\frac{16b}{d} \right) - 1.75 \right] \quad [67]$$

For the surface coil described in Table 5, the theoretical inductance is calculated as $L_{th} = 331 \text{ nH}$. Coil imperfections will, however, likely cause the real coil inductance to deviate from theory. Coil

inductance was measured with a Hewlett Packard 4191A RF impedance analyzer and found to be $L_{\text{exp}} = 280 \text{ nH}$ (see Figure 7).

In addition to the coil inductor there is a stray coil capacitance, C_s [F], caused by electric field resulting from the voltage across the coil terminals, V_{in} . The value of the stray capacitance may be determined from the coil self-resonant frequency. Using an HP 4191A, the *effective* coil inductance versus frequency was measured. The data are displayed in Figure 7. From [26], the stray capacitance may be determined according to

$$C = \frac{1}{\omega^2 L} \quad [68]$$

as $C_s = 4.07 \text{ pF}$. This capacitance must be taken into account whenever equation [26] or its variants are used.

In order to construct resonant surface coil loops, capacitance must be added to the inductive coil circuit. The capacitance required for resonance may be calculated from [68]. The stray coil capacitance must be acknowledged when calculating the capacitance required for resonance. Realizing this, the capacitance required for resonant coils is listed in Table 6. American Technical Ceramics Corporation (47) 100E low-loss transmitter porcelain microstrip capacitors provided the necessary coil capacitance.

The ohmic resistance of the surface coil may be calculated from [33]. Like the coil inductance, the real ohmic resistance may be expected to differ from theoretically calculated values due to imperfections in the coil shape and material. Using an HP 4191A, the experimental ohmic resistance of the coil was measured at the frequencies of theoretical interest. Due to the upper frequency limit of the test equipment, a complete data set was not obtained. However, the data that were obtained are in good agreement with the theoretical ohmic resistance given by [33]. Based on this observation, theoretically calculated values of R_{Ω} will be used. The RF surface coils may be modeled as the electrical circuit shown in Figure 8.

Table 6. The capacitance required for construction of resonant surface coil loops. The effect of the stray coil capacitance ($C_s = 4.07$ pF) is not included in these calculations. If C_s were included, the capacitance becomes negative between 128 MHz and 170 MHz. This is where the coil self-resonant frequency should and does occur (see Figure 7).

B_0 field strength (T)	^1H resonant frequency (MHz)	Discrete capacitance (pF)
0.5	21	200
1.5	64	22
3.0	128	5.5
4.0	170	3.1
4.7	200	2.2
7.0	300	1.0
9.4	400	0.5

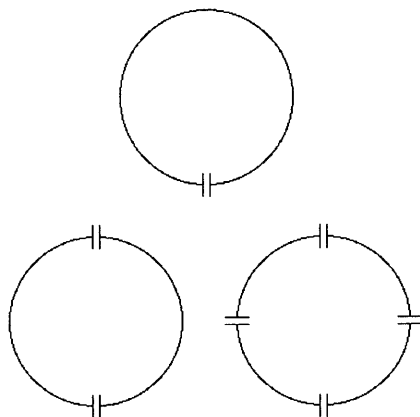


Figure 6. Coil schematic diagrams for the discrete capacitance distributed in one, two, and four locations.

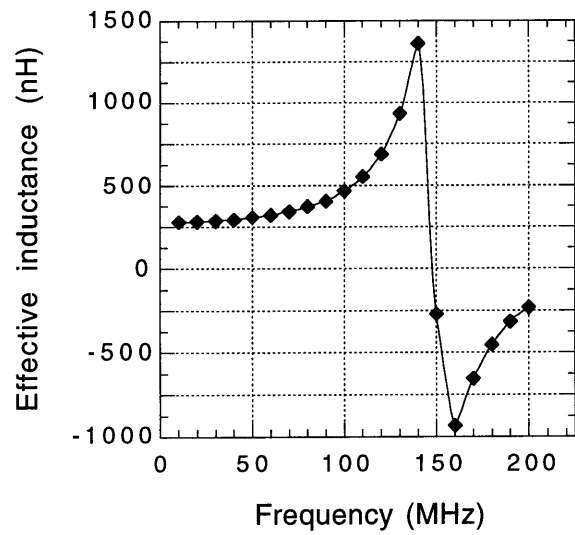


Figure 7. Effective inductance versus frequency for a one-capacitor surface coil. The stray capacitance of the coil may be determined from the resonant point ($L = 0$) according to [68]. Experiment has determined this point as $f_0 = 149$ MHz.

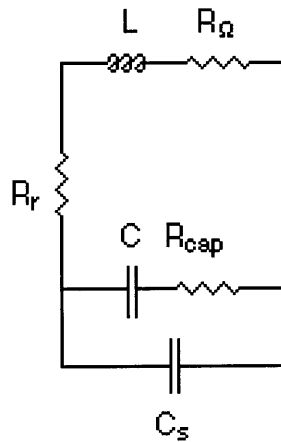


Figure 8. Electrical circuit diagram of the surface coil used in this study. The symbols are defined as follows: L = coil inductance, C = coil capacitance, C_s = stray capacitance, R_Ω = ohmic resistance, R_{cap} = capacitor resistance, and R_r = radiation resistance.

The measurement of interest in this study is the coil Q at the ^1H resonant frequency, in the unloaded and loaded condition. From these data one may determine the coil radiation resistance, load resistance, unloaded and loaded B_1 field magnitude, and unloaded and loaded SNR. All Q measurements were performed on a Hewlett Packard HP 8753C vector network analyzer. To measure the unloaded Q , coils were coupled to a HP 8753C using two small inductive loops as depicted in Figure 9. This method eliminates undesirable secondary resonance peaks observed in the data when capacitively coupling the coil.

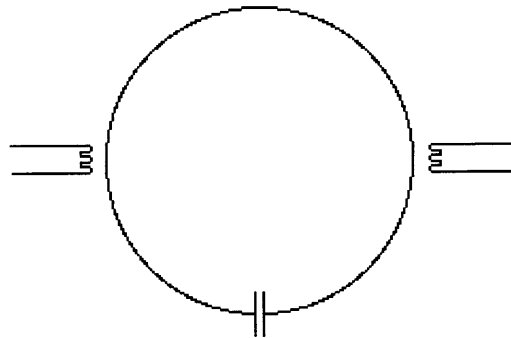


Figure 9. A diagram of the inductive coupling scheme used to measure coil Q .

The input signal originated in Port 1 of the HP 8753C. It was then sent via $50\ \Omega$ coaxial transmission line to a power amplifier [660 mW (35 dB from 1-350 MHz)] used to reduce noise relative to the signal. Next the signal traveled along another $50\ \Omega$ line to the transmitting inductor. The signal returned via the receiving inductor, which was connected by a $50\ \Omega$ line to Port 2 of the HP 8753C. The S_{21} transmission coefficient is the parameter that was measured. During measurements, coils were located atop an electrically insulated platform and isolated from conductive material in the surroundings. Q was measured by the HP 8753C using the algorithm

$$Q = \frac{f_c}{\Delta f_{.3dB}}, \quad [69]$$

where f_c [MHz] is the center frequency and $\Delta f_{.3dB}$ [MHz] is the -3 dB bandwidth about f_c .

For the loaded measurements of Q , a head phantom was constructed. The phantom was a lexan cylinder (height = 4.56 in, diameter = 11.78 in) filled with 7.0 liters of 0.7% (by weight) saline solution to approximate the conductivity of human tissue. The surface coil was placed in a lexan box and fixed to the bottom. The box was then inverted and the head phantom placed atop the box. Measurements were performed in the same manner as described for the unloaded case.

5. RESULTS

Q data were collected with each coil impedance matched to a varying degree from ~ 15 dB to ~ 40 dB. This was done to ensure accuracy while simultaneously keeping the energy transfer at a level that did not load the coil with the inductive couplers. The Q values acquired for each coil were averaged and are displayed in Figures 10 and 11. The averaged Q data is also listed in Appendix B.

From the Q data we may determine the frequency dependence of key parameters. Equation [59] and the experimental inductance permits calculation of the total resistance of both the unloaded and loaded surface coils. These values are listed in Appendix B. For the unloaded coils, the experimentally determined coil inductance, calculated ohmic resistance, and ATC-provided capacitive resistance was used to determine R_r from

$$R_r = R - R_\Omega + R_{cap}, \quad [70]$$

Figure 12 shows the frequency dependence of the coil radiation resistance.

The total resistance calculated from the unloaded and loaded coil Q values may be used to determine the B_1 field magnitude at one coil radius and the dependent coil SNR from equations [64] and [66]. Figures 13 and 14 display the calculated unloaded coil B_1 field strength and SNR while Figures 15 and 16 display the loaded coil B_1 field strength and SNR.

There are numerous potential sources of error in the experiments. However, based on the analysis performed in §6, none of these errors has a significant impact on the data. Error sources include, but are not limited to, the mutual inductance between the coupling probes; the presence of conductive material in the vicinity of the experimental setup; imperfections in the coil that cannot be accounted for, such as the effects of soldering and imperfections in the coil shape and material; and the inherent inaccuracy of the measurement instrumentation.

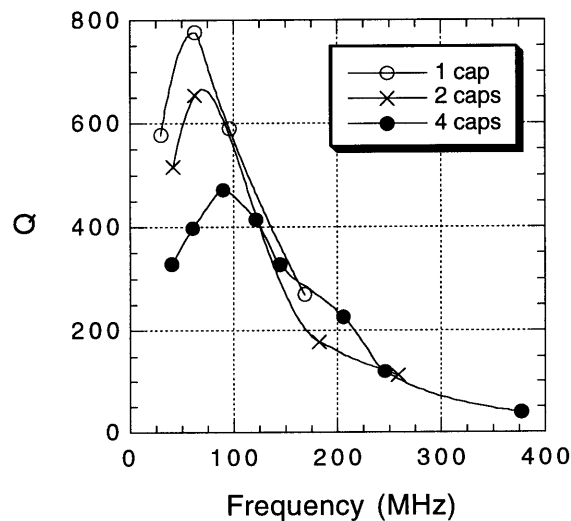


Figure 10. Unloaded Q versus frequency for the surface coils. The legend corresponds to data for coils with capacitance distributed in one, two, and four locations.

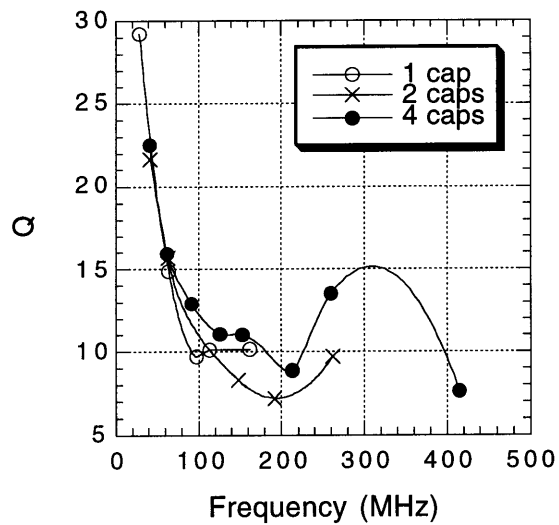


Figure 11. Loaded Q versus frequency for the surface coils. The peak in the data is the result of a dielectric resonance discussed in §6.3.

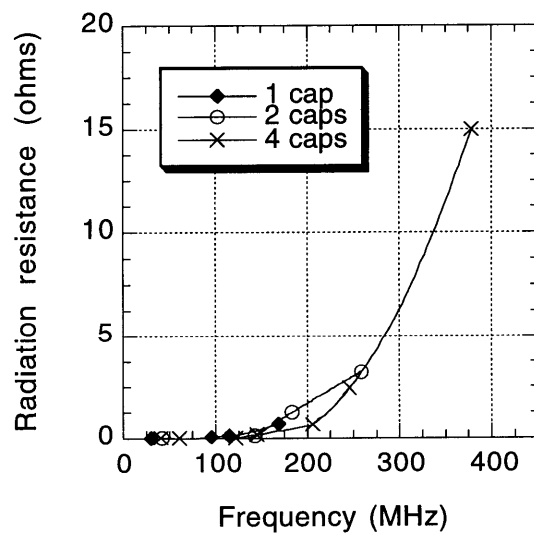


Figure 12. Radiation resistance versus frequency for the surface coils.

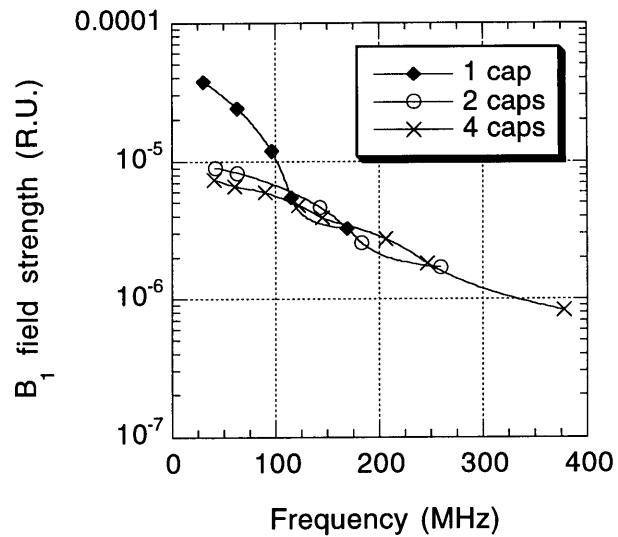


Figure 13. Unloaded B_1 field magnitude at one coil radius versus frequency for the surface coils, calculated from the total coil resistance. The B_1 units are relative to the power input.

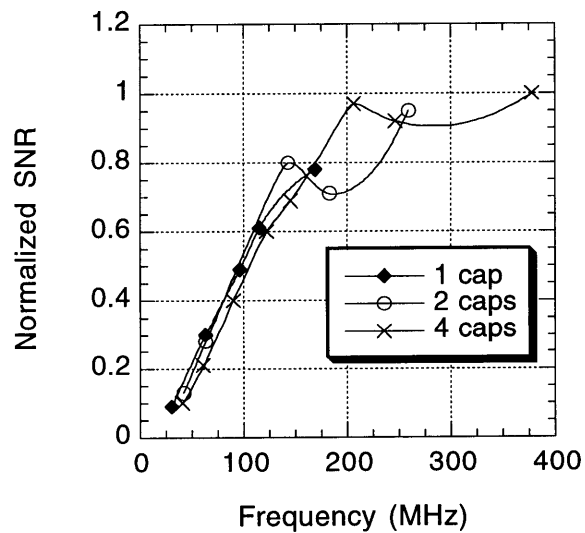


Figure 14. Unloaded, normalized SNR at one coil radius versus frequency for the surface coils.

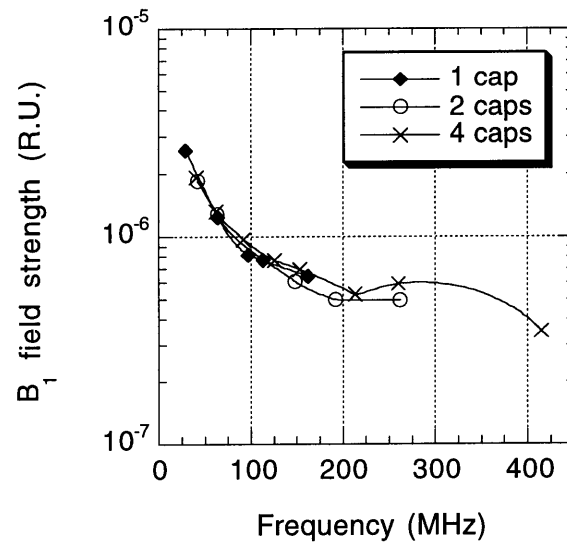


Figure 15. Loaded B_1 field magnitude at one coil radius versus frequency for the surface coils, calculated from the total coil resistance. The B_1 units are relative to the power input.

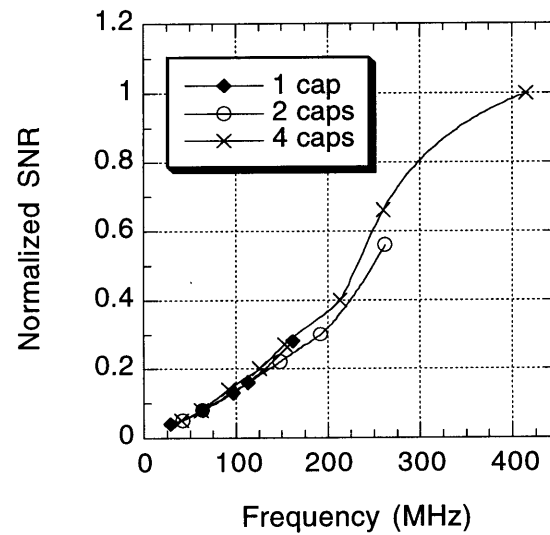


Figure 16. Loaded, normalized SNR at one coil radius versus frequency for the surface coils.

6. DISCUSSION

6.1 COIL Q AND RADIATION RESISTANCE

Figure 17 is a comparison of the calculated and measured coil Q values. Very good agreement can be seen between the theoretical and measured values. The highest Q observed is the measured value of the one-capacitor coil. The subsequent decline in measured Q for the two- and four-capacitor coils may be accounted for by the increase in coil resistance associated with the additional capacitors. At low frequencies, the increase in R_{cap} is a significant fraction of the total coil resistance. The effect becomes imperceptible at higher frequencies as the total resistance of the coil overwhelms the capacitive resistance.

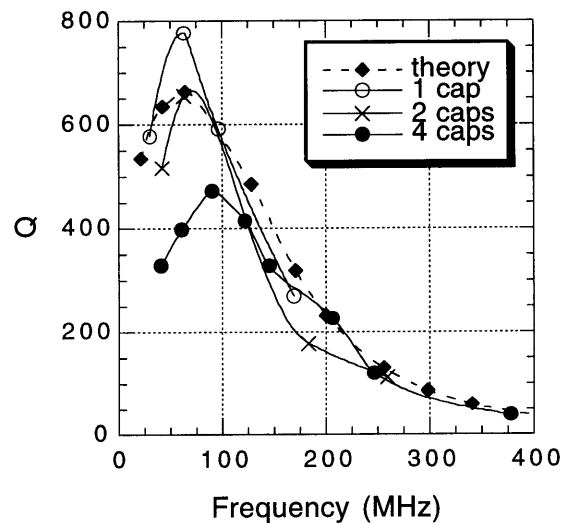


Figure 17. Unloaded coil Q versus frequency for the surface coils. The fact that the one-capacitor coil exceeds theory indicates that measurement error and coil imperfections cause the coil to be less resistive than the theoretical coil.

Figure 18 compares the theoretical and measured radiation resistance of the coil. Only the measured values for the four-capacitor coil are shown, as that is the only coil that resonates at

frequencies high enough to permit comparison. From the plot it may be seen that radiation resistance for a small loop surface coil behaves according to theory. That is,

$$R_r \approx 31,200 \frac{S^2 f^4}{c^4} . \quad [71]$$

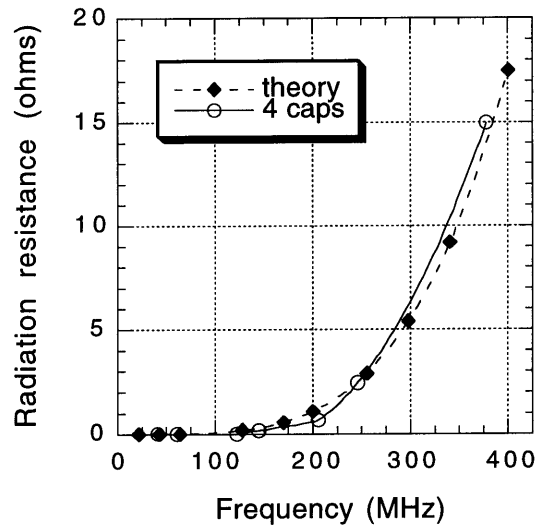


Figure 18. Radiation resistance versus frequency for the theoretical and experimental surface coils. The agreement between the theoretical and experimental values indicates that radiation resistance increases like f_0^4 in a small loop surface coil.

6.2 B_1 FIELD MAGNITUDE AND SNR

Figure 19 is a comparison of the theoretical and measured unloaded B_1 field magnitude at one coil radius from the coil center. The theoretical values were calculated as described in §3.5 and the experimental values were found from [64] using R as determined from the measured Q values. There is excellent agreement between theoretical and experimental values, as would be expected given the accuracy of the R_r measurements.

Figure 20 compares the theoretical and measured SNR of the unloaded surface coils. There is excellent agreement between theory and the real surface coil. SNR may be seen to increase larger than linearly up to 100 MHz. From 100 MHz to 200 MHz, the increase in SNR is approximately linear. Greater than 200 MHz ($D > 0.1\lambda$), the SNR begins to level off due to the rapidly increasing radiation resistance of the coil.

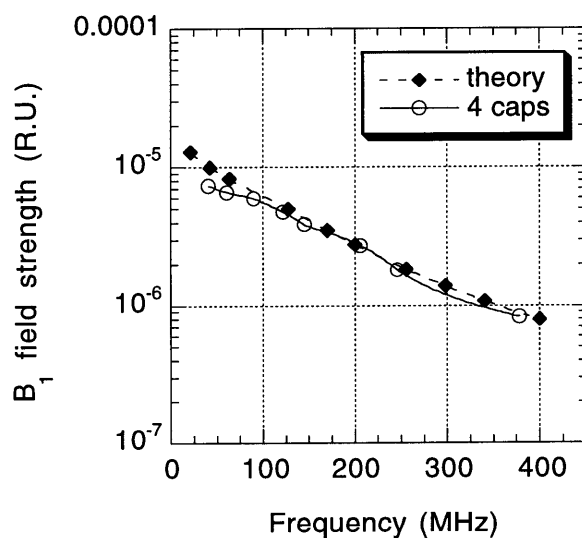


Figure 19. Unloaded B_1 field magnitude at one coil radius versus frequency for the surface coils.

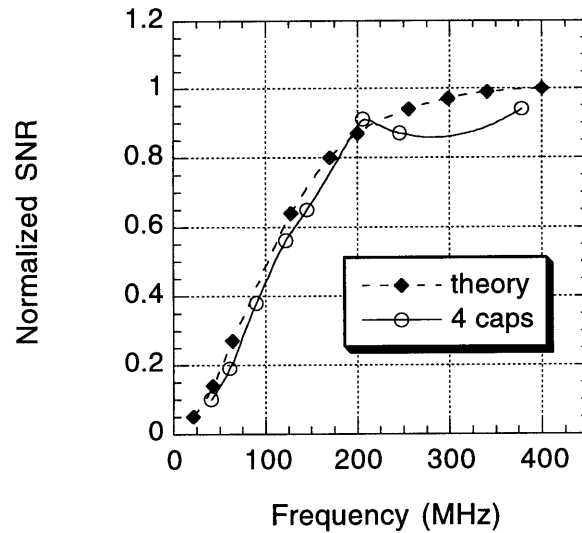


Figure 20. Unloaded, normalized SNR versus frequency for the surface coils. The SNR is normalized to the theoretical maximum value.

6.3 RF COIL DESIGN GUIDELINES

Figure 21 again displays the loaded Q data. The broad peak in the data at ~ 300 MHz is due to a dielectric resonance in the phantom load. The speed of light in saline dictates that the phantom thickness is $\lambda/4$ at ~ 300 MHz. About this frequency energy is preferentially transmitted through the phantom, resulting in higher Q values. The effect of the resonance peak may be expected to appear in any analysis performed with the loaded Q data, including R_L , the loaded B_1 magnitude, and the loaded SNR.

From the previously calculated coil radiation resistance and the measured loaded Q values we may determine the resistance of the phantom load because

$$R_L = R - R_\Omega + R_{\text{cap}} + R_r \quad [72]$$

The frequency dependence of the load resistance is shown in Figure 22. The dip in the load resistance is due to the effect of the dielectric resonance carried through the data analysis. Without

that effect the load resistance appears to increase in a greater than linear fashion as at the lower frequencies.

It is widely believed that the load resistance dominates all other RF losses in biomedical NMR. Based on the measured radiation resistances and load resistances, we now consider this question. Figure 23 shows the load resistance and radiation resistance of a four-capacitor surface coil versus frequency. At 200 MHz ($D \sim 0.1\lambda$) the radiation resistance is a small fraction of the load resistance. At 400 MHz ($D \sim 0.17\lambda$), however, radiation resistance is approximately 20% of the load resistance. Consequently, if radiation resistance was limited in this experimental setup, SNR would increase approximately 8% at 400 MHz. The SNR improvement that would be realized from limiting radiation resistance is shown in Figure 24.

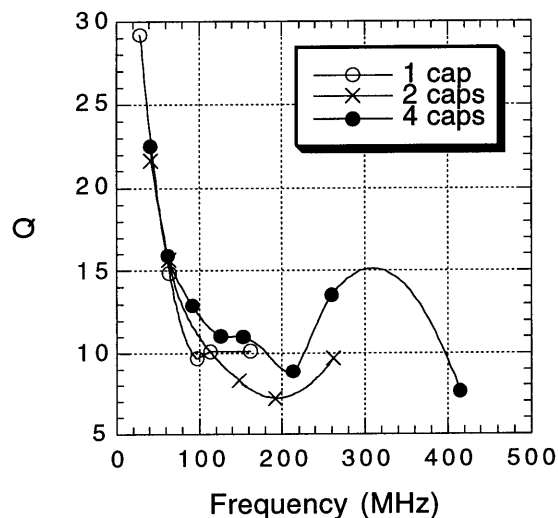


Figure 21. Loaded Q versus frequency for the surface coils. The peak in the data is due to a dielectric resonance that occurs at ~ 300 MHz for the phantom described in § 4.

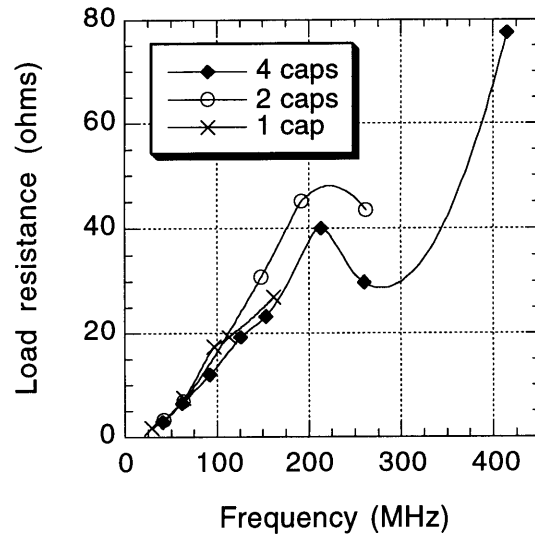


Figure 22. Load resistance versus frequency for the loaded surface coils.

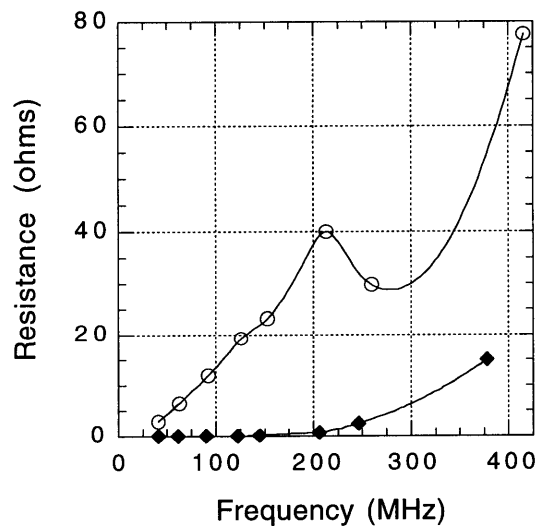


Figure 23. Measured load and radiation resistance versus frequency for the four-capacitor surface coil. While the load resistance is greater than the radiation resistance, the radiation resistance becomes a significant fraction of the load resistance as the electrical length of the coil increases.

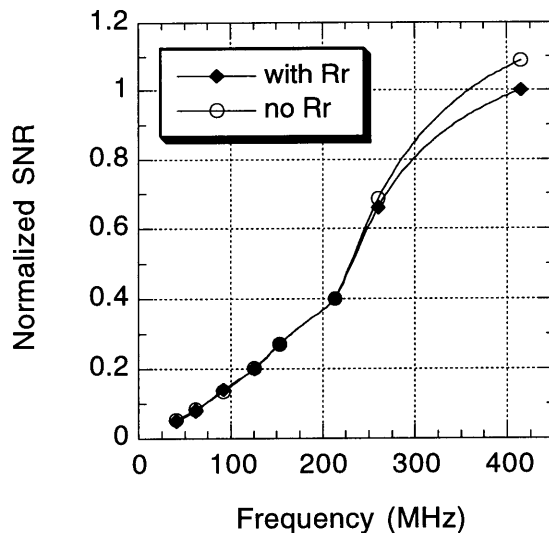


Figure 24. Normalized coil SNR versus frequency for a surface coil both with and without limited radiation resistance. An improvement in SNR is noticeable beginning at 200 MHz ($D \approx 0.1\lambda$) for the radiation-resistance-limited coil.

7. APPLICATIONS

Ackerman *et al.* (50) were the first to utilize surface coils for NMR studies *in-vivo*, applying them to ^{31}P NMR spectroscopy. Since the early investigations of surface coil imaging (51-53), they have become the preferred RF coil for many highly-localized applications (54-81). Their abundance is due in large part to the fact that the circular surface coil offers the best achievable SNR of any RF coil to a limited depth (82,83). Additionally, surface coils are simple and inexpensive to design and construct.

Surface coils are effective because they are very efficient in coupling a small sample volume to its B_1 field (see §3.2). The efficient coupling arises from the physical placement of the coil near the region of interest. Also, the small volume covered by the coil minimizes RF tissue losses and the consequent diminishing of SNR. Surface coils have drawbacks, such as a relatively inhomogeneous B_1 field and a limited field of view (FOV). Also, coil sensitivity decreases sharply with depth in a tissue load. This may be overcome by placing the surface coil inside the patient for

several limited applications. In the end, however, the drawbacks of surface coils are outweighed by the SNR gains realized in many localized applications.

Surface coils may be used *en masse* to form a *phased array* (84). The phased array is a set of overlapping surface coils in which each coil *simultaneously* receives signal from the sample. Each coil signal is then weighted according to the voxel location in the sample. The weighted data are then combined to form a composite image. Phased arrays are commonly used as the receiver coil with a volume coil transmitter, permitting a more homogeneous, and therefore more efficient, B_1 excitation field.

The advantage of the phased array is that it may cover entirely any anatomical structure. This is possible as the coils (elements) that comprise a phased array are decoupled, *i.e.* they do not electrically interact. Thus, the phased array offers the SNR benefit of the surface coil while improving upon the FOV limitation. Further, the insensitivity of surface coils at depth may be overcome by fashioning a phased array volume coil (85). Since the introduction of the phased array, their SNR, FOV, and depth sensitivity benefits have been clearly established (86-95) and they have found numerous applications in biomedical NMR (95-107).

Volume coils are designed to completely surround a sample and are found in NMR scanners in which you may want to image any region of the body. These are generally the most complicated and expensive RF coils, but the challenge of engineering a volume coil is repaid by its highly homogeneous B_1 field and large FOV. The most common volume coil is the *birdcage* coil (108,109).

Most RF coils, including surface coils, phased arrays, and birdcage coils, are designed using lumped-element (RCL) circuit theory. This technique relies on discrete capacitors in the inherently inductive coil circuit to tune the coil to the desired resonant frequency. The coil designed using lumped element theory, while effective at 1.5 T, becomes increasingly inefficient as experiments increase in frequency (36,41,42,110). In many cases, traditional techniques cannot even furnish a coil that can be tuned to the resonant frequency.

The electrical length of RF coils, based on the data collected in this study, increases coil radiation resistance at high frequencies. This renders lumped-element coils ineffective. In order to overcome the problem of radiation resistance in RF coils at high frequencies, one may utilize transverse electromagnetic (TEM) principles, also known as transmission line theory (111). This is the standard design technique when a signal needs to be transmitted with minimal loss. Transmission line theory uses true distributed circuit components, such as transmission lines, strip line circuits, and cavities to theoretically eliminate radiation resistance.

The progression from distributed coil circuits to transmission line principles may be seen in several head and body coils to date (21,112-115). The most capable high-field coil design is the TEM volume coil described by Vaughan (33). This TEM coil shows a significant B_1 -gain improvement over the most common commercial volume coils, including the birdcage coil (41). Its design has been demonstrated successfully in human head and body imaging experiments at 3.0 and 4.0 T (33,116-118) and a head coil (3/5 human scale) has been used to successfully image primates at 9.4 T (119). The TEM coil has also been demonstrated for humans as a body coil at 8 T by Vaughan (120) and as a head coil at 9.4 T by Zhang (121).

The data presented in this study have several implications for RF coil engineering. The link between the coil efficiency and performance and the total coil resistance has been demonstrated. That is, coils are optimized by eliminating resistance. While ohmic resistance (consisting of the coil conductor and the capacitors) and the load resistance are difficult to limit in many cases, coil radiation resistance may be limited. This must be one goal of any attempt to improve high-field RF surface coil performance.

The results for the surface coil used in this study may be applied to surface coils and phased array elements of the same size. However, changing the size of the coil even a few centimeters has important ramifications on the electrical length of the coil. In that case, the lessons learned from this study may be extended to other coils of the same electrical length. The frequencies at which some common coils have the same electrical lengths are listed in Table 7.

Table 7. The frequencies at which various coils have the same electrical length (*i.e.* 0.1λ). Radiative properties of these coils may be expected to be similar based on their electrical length.

Coil type	Coil physical dimension (cm)	Frequency (MHz)
surface coil/phased array element	13	230
surface coil/phased array element	6.5	461
head coil	25	120
body coil	100	30

Equation [71] reveals that decreasing the coil size will limit the coil radiation resistance. Figure 25 compares the radiation resistance of the surface coil used in this study and a surface coil whose radius is half as large. Thus, at 400 MHz the electrical length of the larger surface coil is 0.17λ while the electrical length of the smaller coil is 0.09λ . The radiation resistance of the smaller coil is approximately 95% less than that of the larger coil at 400 MHz. This would translate into a SNR improvement of nearly 4.5 times. Therefore, limiting the electrical wavelength of the RF coil is effective in controlling its radiative properties. Limiting the radiation resistance may also be accomplished by designing coils based on transmission line principles. As their performance indicates, TEM coils are effective in decreasing coil radiation resistance. Coils designed based on transmission line principles may be expected to exhibit a significantly higher Q and SNR.

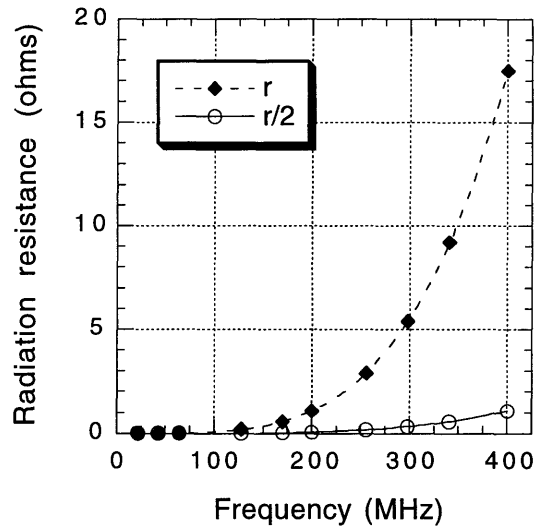


Figure 25. The effect of decreasing surface coil size on radiation resistance. By decreasing the coil radius by 1/2, the resulting effect on radiation resistance may be seen.

8. CONCLUSIONS

The RF losses of a resonant NMR surface coil have been examined for coil electrical lengths from 0.01λ to 0.17λ . The radiation resistance of a small loop surface coil has been shown to increase like f_0^4 . From the measured load and radiation resistances, it has been demonstrated that radiation losses are a significant fraction of the load losses at higher frequencies. This implies that limiting coil radiation resistance may noticeably improve loaded coil SNR.

To prevent radiation resistance one may limit the coil electrical length and/or apply transmission line principles in the construction of RF coils. Decreasing the coil electrical length may be accomplished by limiting the coil size relative to the RF wavelength. Transmission line principles, which have been demonstrated for volume coils, use true distributed circuits to minimize radiation resistance. Based on the data presented, these actions may yield a greater coil

SNR, which may be used to enhance the spatial resolution, temporal resolution, or contrast-to-noise ratio of NMR images.

ACKNOWLEDGEMENTS

The author would like to thank Dr. Patrick Ledden for his help in determining this experiment's setup, aiding with the data interpretation and analysis, and for his efforts to improve the organization, clarity, and content of this paper.

APPENDIX A: ABBREVIATIONS AND SYMBOLS

The abbreviations and symbols used in the paper, in order of their appearance.

Abbreviation or symbol	Definition [SI units]
B_0	static magnetic field strength [T]
NMR	Nuclear Magnetic Resonance
SNR	Signal-to-Noise Ratio
f_0	nuclear resonance frequency [s^{-1} , Hz]
γ	gyromagnetic ratio [MHz/T]
CNR	Contrast-to-Noise Ratio
RF	Radio Frequency; falling between approximately 10 and 10^{12} Hz on the electromagnetic spectrum (47)
R_Ω	ohmic resistance [Ω]
R_r	radiation resistance (relative to the maximum coil current) [Ω]
R_L	resistance due to the coil load [Ω]
ω	angular frequency [rad/s]
$\kappa(\mathbf{r})$	B_1 magnetic field strength per unit current [T/A]
B_1	RF magnetic field strength [T]
R	$R = R_\Omega + R_{cap} + R_r + R_L$ [Ω]
Q	quality factor
λ	wavelength [m]
D	coil diameter [m]

I	nuclear spin [J·s]
I_1	orbital angular momentum [J·s]
s_i	spin angular momentum [J·s]
A	atomic number
I	nuclear spin quantum number
h	Planck's constant; $h = 6.63(10^{-34})$ J·s
I_z	nuclear spin component along the z-axis [J·s]
m_I	$m_I = I, I-1, \dots, 1-I, -I$
$\mu_{I,z}$	nuclear magnetic moment component parallel to the z-axis [$A \cdot m^2$]
E	potential energy [J]
μ	magnetic moment [$A \cdot m^2$]
B	magnetic field [T]
$I(\mathbf{r})$	current [A]
A	magnetic vector potential [N/A^2]
μ_0	permeability of free space; $\mu_0 = 4\pi(10^{-7})$ N/A ²
k	$k^2 = \omega^2 \mu \epsilon$
μ	permeability [N/A^2]
ϵ	permittivity [$C^2/N \cdot m^2$]
r	distance [m]
dl	infinitesimal length element [m]
M	net sample magnetic moment [$A \cdot m^2$]

$\mu_{I,n}$	nuclear magnetic moment [$A \cdot m^2$]
t	time [s]
emf	ElectroMotive Force [V]
E	electric field [V/m]
Z_{in}	input impedance [Ω]
R_{in}	input resistance [Ω]
X_{in}	input reactance [Ω]
P_{in}	input power dissipated [W]
I_{in}	coil current across the coil terminals [A]
P_{Ω}	ohmic power loss [W]
P_r	radiative power loss [W]
X	reactance [Ω]
X_C	capacitive reactance [Ω]
X_L	inductive reactance [Ω]
C	capacitance [F]
L	inductance [H]
R_n	radiation resistance (relative to the current across the coil terminals) [Ω]
ℓ	wire length [m]
a	wire radius [m]
R_s	coil surface resistance [Ω]
σ	conductivity [$\Omega^{-1} \cdot m^{-1}$]

R_{cap}	capacitor resistance [Ω]
\mathcal{S}	instantaneous Poynting vector [W/m^2]
\mathcal{E}	instantaneous electric field intensity [V/m]
\mathcal{H}	instantaneous magnetic field intensity [A/m]
\mathcal{P}	total instantaneous power [W]
ds	$ds = (\hat{n})da$ [m^2]
\hat{n}	unit normal to a surface
da	infinitesimal area element [m^2]
\mathbf{H}	complex magnetic field [A/m]
\mathbf{S}_{av}	time average Poynting vector [W/m^2]
P_{av}	average radiated power [W]
I	coil current [A]
S	coil area [m^2]
c	speed of light in free space; $c = 3(10^8)$ m/s
\mathbf{J}_c	conduction current density [A/m^2]
\mathbf{D}	electric flux density [C/m^2]
\mathbf{J}_d	displacement current density [A/m^2]
σ_L	load conductivity [$\Omega^{-1} \cdot \text{m}^{-1}$]
ϵ_L	load permittivity [$\text{C}^2/\text{N} \cdot \text{m}^2$]
ϕ	scalar potential [V]
V_{in}	voltage across the coil terminals [V]
\hat{r}	unit vector between the point of calculation and a field point [m]
b	coil radius [m]
d	wire diameter [m]
L_{th}	theoretical inductance [H]

L_{exp}	measured inductance [H]
C_s	stray capacitance [F]
f_c	center frequency [MHz]
$\Delta f_{-3\text{dB}}$	-3 dB bandwidth [MHz]
FOV	Field Of View
TEM	Transverse ElectroMagnetic

APPENDIX B: Q DATA

Unloaded Q data.

Frequency (MHz)	Capacitance (pF)	Q_{avg} *	R^{**} (Ω)
30	100	578	0.091
63	22	777	0.143
96	8.2	590	0.286
115	5.6	519	0.390
169	2.2	270	1.101
42	2 × 100	517	0.143
63	2 × 47	655	0.169
143	2 × 8.2	464	0.542
183	2 × 5.6	178	1.805
259	2 × 2.2	112	4.056
41	4 × 220	328	0.216
61	4 × 100	398	0.265
90	4 × 47	472	0.329
122	4 × 27	414	0.508
145	4 × 18	327	0.765
206	4 × 8.2	227	1.566
246	4 × 5.6	120	3.523
378	4 × 2.2	39	16.747

* Q data was averaged over a range of match levels

** R is calculated using equation [59] and the measured coil inductance

Loaded Q data.

Frequency (MHz)	Capacitance (pF)	Q_{avg}	R (Ω)
29	100	29.2	1.747
64	22	14.9	7.574
97	8.2	9.7	17.593
113	5.6	10.1	19.683
162	2.2	10.2	28.079
42	2×100	21.7	3.413
63	2×47	15.7	7.082
148	2×8.2	8.3	31.371
192	2×5.6	7.2	46.914
262	2×2.2	9.7	47.519
41	4×220	22.5	3.149
62	4×100	16.0	6.717
92	4×47	12.9	12.323
126	4×27	11.1	19.702
153	4×18	11.0	24.033
213	4×8.2	8.9	41.586
260	4×5.6	13.5	33.278
415	4×2.2	7.6	94.351

REFERENCES

1. D Stiller, B Gaschler-Markefski, F Baumgart, F Schindler, C Tempelmann, H J Heinze, H Scheich, Lateralized processing of speech prosodies in the temporal cortex: a 3-T functional magnetic resonance imaging study. *Magn Reson Mater Phys Biol M* **5**, 275-284 (1997).
2. D Bavelier, D Corina, P Jezzard, S Padmanabhan, V P Clark, A Karni, A Prinster, A Braun, A Lalwani, J P Rauschecker, R Turner, H Neville, Sentence reading: A functional MRI study at 4 tesla. *J Cognitive Neurosci* **9**, 664-686 (1997).
3. A K Percy, J B Lane, J W Pan, H P Hetherington, Rett syndrome: H-1 spectroscopic imaging at 4.1 tesla. *Ann Neurol* **42**, 34 (1997).
4. B G Goodyear, J S Gati, R S Menon, The functional scout image: Immediate mapping of cortical function at 4 tesla using receiver phase cycling. *Magn Reson Med* **38**, 183-186 (1997).
5. G A Tagaris, S G Kim, J P Strupp, P Andersen, K Ugurbil, A P Georgopoulos, Mental rotation studied by functional magnetic resonance imaging at high field (4 tesla): Performance and cortical activation. *J Cognitive Neurosci* **9**, 419-432 (1997).
6. I Yamada, Y Murata, Y Izumi, T Kawano, M Endo, T Kuroiwa, H Shibuya, Staging of esophageal carcinoma in vitro with 4.7- MR imaging. *Radiology* **204**, 521-526 (1997).
7. R Kuzniecky, H Hetherington, J Pan, J Hugg, C Palmer, F Gilliam, E Faught, R Morawetz, Proton spectroscopic imaging at 4.1 tesla in patients with malformations of cortical development and epilepsy. *Neurology* **48**, 1018-1024 (1997).
8. R Gruetter, M Garwood, K Ugurbil, E R Seaquist, Observation of resolved glucose signals in H-1 NMR spectra of the human brain at 4 Tesla. *Magn Reson Med* **36**, 1-6 (1996).
9. J W Pan, G F Mason, G M Pohost, H P Hetherington, Spectroscopic imaging of human brain glutamate by water-suppressed J-refocused coherence transfer at 4.1 T. *Magn Reson Med* **36**, 7-12 (1996).
10. J W Pan, H P Hetherington, J T Vaughan, G Mitchell, G M Pohost, J N Whitaker, Evaluation of multiple sclerosis by H-1 spectroscopic imaging at 4.1 T. *Magn Reson Med* **36**, 72-77 (1996a).
11. J W Pan, J T Vaughan, T K Kuzniecky, G M Pohost, H P Hetherington, High resolution neuroimaging at 4.1 T. *Magn. Reson. Imaging* **13**(7), 915 (1995).
12. H P Hetherington, J W Pan, G F Mason, D Adams, M J Vaughn, D B Twieg, G M Pohost, Quantitative H-1 spectroscopic imaging of human brain at 4.1 T using image segmentation. *Magn Reson Med* **36**, 21-29 (1996).
13. H Hetherington, T Kuzniecky, J Pan, G Mason, R Morawetz, C Harris, E Faught, T Vaughan, G Pohost, Proton nuclear-magnetic-resonance spectroscopic imaging of human temporal-lobe epilepsy at 4.1 T. *Ann Neurol* **38**, 396-404 (1995).
14. H P Hetherington, D J E Luney, J T Vaughan, J W Pan, S L Ponder, O Tschendel, D B Twieg, G M Pohost, 3D P-31 spectroscopic imaging of the human heart at 4.1-T. *Magn Reson Med* **33**, 427 (1995a).

15. S G Kim, X P Hu, G Adriany, K Ugurbil, Fast interleaved echo-planar imaging with navigator: High resolution anatomic and functional images at 4 Tesla. *Magn Reson Med* **35**, 895-902 (1996).
16. S Duewell, S D Wolff, H Wen, R S Balaban, P Jezzard, MR imaging contrast in human brain tissue: Assessment and optimization at 4 T. *Radiology* **199**, 780-786 (1996).
17. P Mansfield, R Coxon, J Hykin, Echo-volumar imaging (EVI) of the brain at 3.0 T--First normal volunteer and functional imaging results. *J Comput Assist Tomogr* **19**, 847-852 (1995).
18. A E Stillman, X Hu, M Jeroschherold, Functional MRI of brain during breath-holding at 4-T. *Magn Reson Med* **13**, 893-897 (1995).
19. J H Lee, M Garwood, R Menon, G Adriany, P Andersen, C L Truwit, K Ugurbil, High-contrast and fast 3-dimensional magnetic-resonance-imaging at high fields. *Magn Reson Med* **34**, 308-312 (1995).
20. R S Menon, S Ogawa, X P Hu, J P Strupp, P. Anderson, K Ugurbil, BOLD based functional MRI at 4-Tesla includes a capillary bed contribution--Echo-planar imaging correlates with previous optical imaging using intrinsic signals. *Magn Reson Med* **33**, 453-459 (1995).
21. K Ugurbil, M Garwood, J Ellermann, K Hendrich, R Hinke, X Hu, S Kim, R Menon, H Merkle, S Ogawa, R Salmi, Imaging at high magnetic fields: Initial experiences at 4 T. *Magn Reson Quarterly* **9(4)**, 259 (1993).
22. H Barfuss, H Fischer, D Hentschel, R Ladebeck, A Oppelt, R Wittig, W Duerr, R Oppelt, In vivo magnetic resonance imaging and spectroscopy of humans with a 4 T whole-body magnet. *NMR Biomed* **3**, 31 (1990).
23. D I Hoult, P C Lauterbur, The sensitivity of the zeugmatographic experiment involving human samples. *J Magn Reson* **34**, 425 (1979).
24. Personal communication with J T Vaughan.
25. E M Purcell, H C Torrey, R V Pound, Resonance absorption by nuclear magnetic moments in a solid. *Phys Rev* **69**, 37 (1946).
26. F Bloch, W W Hansen, M E Packard, Nuclear induction. *Phys Rev* **69**, 127 (1946).
27. P C Lauterbur, Image formation by induced local interaction: Examples employing nuclear magnetic resonance. *Nature* **242**, 190 (1973).
28. P Mansfield, P K Grannell. *J Phys C* **6**, L422 (1973).
29. R V Damadian, Apparatus and method for detecting cancer in tissue, U.S. Patent 3,789,832 (1974).
30. P Mansfield, I L Pykett, P G Morris, R E Coupland. *Br J Radiol* **51**, 921 (1978).
31. J F Schenck, C L Dumoulin, R W Redington, H Y Dressel, T T Elliott, I L McDougall, Human exposure to 4.0-Tesla magnetic fields in a whole-body scanner. *Med Phys* **19(4)**, 1089 (1992).

32. J Vetter, G Ries, T Reichert, A 4-tesla superconducting whole-body magnet for MR imaging and spectroscopy. *IEEE Trans Magn* **24**, 1285-1287 (1988).
33. J T Vaughan, H P Hetherington, J O Otu, J W Pan, G M Pohost, High frequency volume coils for clinical NMR imaging and spectroscopy. *Magn Reson Med* **32**, 206 (1994).
34. J Jackson, "Classical electrodynamics," Wiley, New York, 1975.
35. W L Stutzman, G A Thiele, "Antenna Theory and Design," John Wiley & Sons, New York, 1981.
36. M D Harpen, Radiative losses of a birdcage resonator. *Magn Reson Med* **29**, 713-716 (1993).
37. O Ocali, E Atalar, Importance of radiation loss on noise of MR imaging surface coils. Supplement to *Radiology* **201**, 292 (1996).
38. J T Vaughan, D N Haupt, P J Noa, J M Vaughn, G M Pohost, RF front-end for a 4.1-tesla clinical NMR spectrometer. *IEEE Trans Nucl Sci* **42**, 1333-1337 (1995).
39. J T Vaughan, P Röschmann, J W Pan, H P Hetherington, B L W Chapman, P Nos, J Vermeulen, G M Pohost, A double resonant surface coil for 4.1 tesla whole body NMR, in "Book of Abstracts, SMRM, Berkeley, 1991," p. 722.
40. J T Vaughan, J Harrison, B L W Chapman, J W Pan, H P Hetherington, J Vermeulen, W T Evanochko, G M Pohost, High field/low field comparisons of rf field distribution, power deposition, and S/N for human NMR: preliminary results at 4.1 T, in "Book of Abstracts: Works in Progress, SMRM, Berkeley, 1991a," p. 1114.
41. J T Vaughan, An RF volume coil comparison study: 1.5 T to 9.4 T, in "Proc., ISMRM, 1998."
42. J M Jin, J Chen, On the SAR and field inhomogeneity of birdcage coils loaded with the human head. *Magn Reson Med* **38**, 953-963 (1997).
43. J Jin, G Shen, T Perkins, On the field inhomogeneity of the birdcage coil. *Magn Reson Med* **32**, 418-422 (1994).
44. K S Krane, "Introductory Nuclear Physics," John Wiley & Sons, New York, 1988.
45. K H Hausser, H R Kalbitzer, "NMR in Medicine and Biology," Springer-Verlag, Berlin, 1991.
46. C A Balanis, "Antenna Theory: Analysis and Design," Harper & Row, New York, 1982.
47. American Technical Ceramics Corporation; One Norden Lane; Huntington Station, New York 11746-2102; tel: 516.547.5700.
48. R F Harrington, "Time-harmonic Electromagnetic Fields," McGraw-Hill, New York, 1961.
49. P A Tipler, "Physics for Scientists and Engineers," Worth Publishers, New York, 1991.

50. J J H Ackerman, T H Grove, G G Wong, D G Gadian, G K Radda, Mapping of metabolites in whole animals by ^{31}P NMR using surface coils. *Nature* **283**, 167-170 (1980).
51. M L Bernardo, A J Cohen, P C Lauterbur, Radiofrequency coil designs for nuclear magnetic resonance magnetic resonance tomographic imaging, in *IEEE proceedings of the international workshop on physics and engineering in medical imaging*, March 1982: 277-284.
52. S J El Yousef, R J Alfidi, R H Duchesneau, *et al.*, Initial experience with nuclear magnetic resonance (NMR) imaging of the human breast. *J Comput Assist Tomogr* **7**, 215-218 (1983).
53. L Axel, Surface coil magnetic resonance imaging. *J Comput Assist Tomogr* **8**, 381-384 (1984).
54. G Chaljub, C R Hamilton, E VanSonnenberg, G R Wittich, MR imaging guided percutaneous biopsy and tumor localization utilizing 5 inch surface coil. Supplement to *Radiology* **205**, 278 (1997).
55. A Qayyum, J E Husband, D A MacVicar, A R Padhani, P Revell, Surface coil MR imaging of brachial plexopathy in breast cancer. Supplement to *Radiology* **205**, 1675 (1997).
56. S Kageyama, T Ueda, R Kushima, T Sakamoto, Primary adenosquamous cell carcinoma of the male distal urethra: Magnetic resonance imaging using a circular surface coil. *J Urol* **158**, 1913-1914 (1997).
57. Y Naito, M Miura, K Funabiki, E Naito, I Honjo, Application of parasagittal surface coil MRI to otoneurological diagnosis. Supplement 528 to *Acta Oto-Laryngol*, 85-90 (1997).
58. H Demachi, O Matsui, K Hoshiba, M Kimura, S Miyata, Y Kuroda, K Konishi, M Tsuji, A Miwa, Dynamic MRI using a surface coil in chronic cholecystitis and gallbladder carcinoma: Radiologic and histopathologic correlation. *J Comput Assist Tomogr* **21**, 643-651 (1997).
59. N Hosten, A J Lemke, B Sander, R Wassmuth, K Terstegge, N Bornfeld, R Felix, MR anatomy and small lesions of the eye: Improved delineation with a special surface coil. *European Radiol* **7**, 459-463 (1997).
60. M J Kim, J J Chung, Y H Lee, J T Lee, H S Yoo, Comparison of the use of the transrectal surface coil and the pelvic phased-array coil in MR imaging for preoperative evaluation of uterine cervical carcinoma. *Amer J Roentgenol* **168**, 1215-1221 (1997).
61. V L Doyle, G S Payne, D J Collins, M W Verrill, M O Leach, Quantification of phosphorus metabolites in human calf muscle and soft-tissue tumours from localized MR spectra acquired using surface coils. *Phys Med Biol* **42**, 691-706 (1997).
62. M J Kim, J T Lee, M S Lee, J S Suh, H S Yoo, MR imaging of male infertility with an endorectal surface coil. *Abdom Imaging* **22**, 348-353 (1997a).
63. P E Grant, A J Barkovich, L L Wald, W P Dillon, K D Laxer, D B Vigneron, High-resolution surface-coil MR of cortical lesions in medically refractory epilepsy: A prospective study. *Amer J Neuroradiol* **18**, 291-301 (1997).
64. J M Silverman, T L Krebs, MR imaging evaluation with a transrectal surface coil of local recurrence of prostatic cancer in men who have undergone radical prostatectomy. *Amer J Roentgenol* **168**, 379-385 (1997).

65. H Hasegawa, T Teramoto, M Watanabe, Y Imai, M Muaki, S Kodaira, M Kitajima, Diffuse cavernous hemangioma of the rectum: MR imaging with endorectal surface coil and sphincter-saving surgery. *J Gastroenterology* **31**, 875-879 (1996).
66. J J Vaquero, M Rivera, A Santos, J RuizCabello, F DelPozo, MR imaging visualization of small structures with improved surface coils. Supplement to *Radiology* **201**, 292 (1996).
67. G Chaljub, R F LaPrade, C Hamilton, J J Heinemann, F A Wentorf, MR imaging of the posterolateral aspect of the knee: Use of a 5-inch surface coil. Supplement to *Radiology* **201**, 531 (1996).
68. R Friedrichs, T Ebert, T J Vogl, H Lobeck, H J Scholman, Use of endorectal surface coil magnetic resonance imaging for diagnosis of a multicystic seminal vesicle with ipsilateral renal agenesis. *Urol Int* **57**, 115-118 (1996).
69. H Gruber, M Rauchenwald, E Breinl, P Reittner, H Trummer, The role of endorectal surface-coil MRI in the diagnosis of ectopic insertion of the ureter into a seminal vesicle cyst. *Brit J Urol* **78**, 306 (1996).
70. K W Preidler, K Tamussino, D M Szolar, G Ranner, F Ebner, Staging of cervical carcinomas--Comparison of body-coil magnetic resonance imaging and endorectal surface coil magnetic resonance imaging with histopathologic correlation. *Invest Radiol* **31**, 458-462 (1996).
71. R A H Boni, C Meyenberger, J P Lundquist, F Trinkler, U Lutolf, G P Krestin, Value of endorectal coil versus body coil MRI for diagnosis of recurrent pelvic malignancies. *Abdom Imaging* **21**, 345-352 (1996).
72. S Ozawa, Y Imai, N Ando, M Ueda, M Kitajima, New magnetic resonance imaging of esophageal cancer using an endoluminal surface coil. Supplement to *Gastroenterology* **110**, A573 (1996).
73. N Hosten, A Lemke, B Sander, H Requardt, R Wassmuth, J Maurer, N Anders, R Felix, MRT of the eye: Normal anatomy and detection of minute lesions via a high-resolution surface coil. *Fortschr Rontgenstrahl Neuen* **164**, 126-131 (1996).
74. V Nicolas, M S Beese, C H Lund, S. Joobmann, P Hammerer, H Henke, Endorectal surface coil MR imaging: Staging and volumetry of prostate cancer. Supplement to *Radiology* **197**, 254 (1995).
75. K S Cho, K M Kim, C W Mun, S T Kim, Y H Auh, R F Mattrey, Endovaginal surface coil MR-imaging of uterine cervical-carcinoma: Comparison with conventional body coil MR-imaging. Supplement to *Radiology* **197**, 321 (1995).
76. Y Naito, I Honjo, H Takahashi, Y Shiomi, E Naito, K Nishimura, Y Sakaguchi, Surface-coil magnetic-resonance-imaging of the internal auditory-canal and the inner-ear. *Ann Otol Rhinol Laryngol* **104**, 776-782 (1995).
77. J D Tesorotess, A Amoruso, D Rovini, L Balzarini, E Ceglia, E Civelli, G Trecate, T Savio, R Musumeci, Microcalcifications in clinically normal breast--The value of high-field, surface coil, Gd-DTPA-enhanced MRI. *European Radiol* **5**, 417-422 (1995).

78. M Mullerschimpfle, H Franz, B Lobinger, C D Claussen, High-resolution MR-imaging of the anal-sphincter using an intravaginal surface coil. *Fortschr Rontgenstrahl Neuen* **162**, 478-481 (1995).
79. D D Dodai, R A Youngberg, MRI of the hip with a shoulder surface coil in off-coronal plane. *J Comput Assist Tomogr* **19**, 336-338 (1995).
80. G Brinkmann, U H Melchert, L Emde, H Wolf, C Muhle, J Brossman, M Reuter, M Heller, In-vivo P-31-MR-spectroscopy of focal hepatic-lesions--Effectiveness of tumor-detection in clinical-practice and experimental studies of surface coil characteristics and localization technique. *Invest Radiol* **30**, 56-63 (1995).
81. F Cornud, X Belin, P Melki, O Helenon, Y Cretien, B Dufour, J F Moreau, MRI of prostate zonal anatomy with an endorectal surface coil. *J Radiol* **76**, 11-20 (1995).
82. W A Edelstein, T H Foster, J H Schenck, in "SMRM, 4th Annual Meeting, 1985," p. 964.
83. P B Roemer, W A Edelstein, in "SMRM, 6th Annual Meeting, 1987," p. 410.
84. P B Roemer, W A Edelstein, C E Hayes, S P Souza, O M Mueller, The NMR phased array. *Magn Reson Med* **16**, 192 (1990).
85. C E Hayes, N Hattes, P B Roemer, Volume imaging with MR phased arrays. *Magn Reson Med* **18**, 309 (1991).
86. L H Schwartz, D M Panicek, E Thomson, S K Herman, G V Shah, R T Heelan, Y Fong, L H Blumgart, Comparison of phased-array and body coils for MR imaging of liver. *Clin Radiol* **52**, 745-749 (1997).
87. C E Hayes, J S Tsuruda, C M Mathis, K R Maravilla, M Kliot, A G Filler, Brachial plexus: MR imaging with a dedicated phased array of surface coils. *Radiology* **203**, 286-289 (1997).
88. J Scheidler, A F Heuck, R Bruening, P Kohz, R Kimmig, M K Stehling, M F Reiser, Magnetic resonance imaging of the female pelvis--New circularly polarized body array coil versus standard body coil. *Invest Radiol* **32**, 1-6 (1997).
89. M Niitsu, H Mishima, S Miyakawa, Y Itai, High resolution MR imaging of the bilateral hips with dual phased-array. *J Magn Reson Imaging* **6**, 950-953 (1996).
90. J M Wang, A Reykowski, J Dickas, Calculation of the signal-to-noise ratio for simple surface coils and arrays of coils. *IEEE Trans Biomed Engr* **42**, 908-917 (1995).
91. J Breslau, R W Dalley, J S Tsuruda, C E Hayes, K R Maravilla, Phased-array surface coil MR of the orbits and optic nerves. *Amer J Neuroradiol* **16**, 1247-1251 (1995).
92. N G Campeau, C D Johnson, J P Felmlee, J N Rydberg, R K Butts, R L Ehman, S J Riederer, MR-imaging of the abdomen with a phased-array multicoil--Prospective clinical evaluation. *Radiology* **195**, 769-776 (1995).
93. P Schmalbrock, J Pruski, L Sun, A Rao, J W Monroe, Phased-array RF coils for high-resolution MRI of the inner-ear and brain-stem. *J Comput Assist Tomogr* **19**, 8-14 (1995).
94. C E Hayes, J S Tsuruda, C M Mathis, Temporal lobes--Surface MR coil phased-array imaging. *Radiology*, **189**, 918-920 (1993).

95. C E Hayes, M J Dietz, B F King, R L Ehman, Pelvic imaging with phased-array coils--Quantitative assessment of signal-to-noise ratio improvement. *J Magn Reson Imaging* **2**, 321-326 (1992).
96. S E Moyher, L L Wald, S J Nelson, D Hallam, W P Dillon, D Norman, D B Vigneron, High resolution T2-weighted imaging of the human brain using surface coils and an analytical reception profile correction. *J Magn Reson Imaging* **7**, 512-517 (1997).
97. D H Lewis, P Ory, M D Holmes, A Wilensky, C Dodrill, W A Cohen, L M Ojemann, G A Ojemann, High resolution interictal SPECT and phased array MRI: EEG localization comparison in partial epilepsy diagnosis. Supplement to *J Nucl Med* **38**, 339 (1997).
98. T Fujita, K Honjo, K Ito, T Matsumoto, N Matsunaga, B Hamm, High-resolution dynamic MR imaging of hepatocellular carcinoma with a phased array body coil. *Radiographics* **17**, 315-331 (1997).
99. C E Hayes, C M Mathis, C Yuan, Surface coil phased arrays for high-resolution imaging of the carotid arteries. *J Magn Reson Imaging* **1**, 109-112 (1996).
100. S Sironi, F DeCobelli, A Zerbi, E Angeli, G Balzano, G Taccagni, V DiCarlo, A DelMaschio, Pancreatic adenocarcinoma: Assessment of vascular invasion with high-field MR imaging and a phased-array coil. *Amer J Roentgenol* **167**, 997-1001 (1996).
101. L L Wald, S E Moyher, M R Day, S J Nelson, D B Vigneron, Proton spectroscopic imaging of the human brain using phased array detectors. *Magn Reson Med* **34**, 440-445 (1995).
102. B L Buff, C S Zuo, H E Longmaid, R L Jenkins, P A Wielopolski, M E Clouse, MR cholangiopancreatography: Fast imaging techniques with a phased-array coil. Supplement to *Radiology* **197**, 312 (1995).
103. K Ito, K Honjo, T Fujita, H Awaya, N Matsunaga, R F Mattrey, High-resolution dynamic contrast-enhanced MR-imaging of the uterus with a new phased-array multicoil. Supplement to *Radiology* **197**, 509 (1995).
104. T Fujita, K Honjo, K Ito, T Matsumoto, H Awaya, N Matsunaga, Normal anatomy of the mediastinum and hilus of the lung and tumor-detection: Findings from high-resolution MR-imaging with a phased-array surface coil. Supplement to *Radiology* **197**, 527 (1995).
105. G Tan, W Song, A Jesmanowicz, J S Hyde, T Raidy, S J Li, Multi-channel magnetic resonance spectroscopy, in "Proc., SMRM 12th Annual Meeting, New York, 1993," pp.370.
106. R Kier, S McCarthy, T R McCauley, R C Smith, S Schiff, B Lytton, Fast SE MR imaging of prostate-cancer with a pelvic phased-array coil. *Radiology* **185**, 275 (1992).
107. C J Hardy, P A Bottomley, K W Rohling, P B Roemer, An NMR phased array for human cardiac 31-P spectroscopy. *Magn Reson Med* **28** 54-64 (1992).
108. C E Hayes, W A Edelstein, J F Schenck, O M Mueller, M Eash, An efficient, highly homogeneous radiofrequency coil for whole-body NMR imaging at 1.5 T. *J Magn Reson* **63**, 622-628 (1985).
109. J Tropp, The theory of the bird-cage resonator. *J Magn Reson* **82**, 51-62 (1989).

110. G Adriany, J T Vaughan, P Andersen, H Merkle, M Garwood, K Ugurbil, Comparison between head volume coils at high field, *in* "Proc., SMRM, 1995," p. 971.
111. R A Chipman, "Theory and Problems of Transmission Lines," McGraw-Hill, New York, 1968.
112. D W Alderman, D M Grant, An efficient decoupler coil design which reduces heating in conductive samples in superconducting spectrometers. *J Magn Reson* **36**, 477 (1979).
113. H J Schneider, P Dullenkopf, Slotted tube resonator: A new NMR probe head at high observing frequencies. *Rev Sci Instrum* **48**, 68 (1997).
114. J F Bridges, Cavity resonator with improved magnetic field uniformity for high frequency operation and reduced dielectric heating in NMR imaging devices, U.S. Patent 4,751,464 (1988).
115. P K Röschmann, High-frequency coil system for a magnetic resonance imaging apparatus, U.S. Patent 4,746,866 (1988).
116. J T Vaughan, H P Hetherington, J G Harrison, J O Otu, J W Pan, P J Noa, G M Pohost, High frequency coils for clinical nuclear magnetic resonance and spectroscopy. *Physica Medica* **IX**, 147 (1993).
117. J T Vaughan, H P Hetherington, G M Pohost, Multiply tuned, high frequency volume coils for clinical NMR, *in* "Proc., Soc. Magn. Reson., 1994a," p. 1119.
118. J T Vaughan, High frequency volume coils for nuclear magnetic resonance applications, U.S. Patent 5,557,247 (1996).
119. J T Vaughan, M Garwood, H Merkle, G Adriany, R M Uckun, K Ugurbil, First 9.4 T homogeneous head imaging of a monkey, *in* "Proc., 82nd RSNA, 1996a," **890**, 292.
120. J T Vaughan, *et al.*, A high frequency body coil for clinical NMR, *in* "Proc., Soc. Magn. Reson., 1994b," p. 1113.
121. N Zhang, M S Toos, J T Vaughan, S T S Wong, T F Budinger, Head coil B-1 field homogeneity and SNR performance at 8-10 T, *in* "Proc., Soc. Magn. Reson., 1996," p. 252.